nature cell biology

Innate control of actin nucleation determines two distinct migration behaviours in dendritic cells

Pablo Vargas[1,2,9], Paolo Maiuri[2,8], Marine Bretou[1,8], Pablo J. Sáez[1], Paolo Pierobon[1], Mathieu Maurin[1], Mélanie Chabaud[1], Danielle Lankar[1], Dorian Obino[1], Emmanuel Terriac[2], Matthew Raab[2], Hawa-Racine Thiam[2], Thomas Brocker[3], Susan M. Kitchen-Goosen[4], Arthur S. Alberts[4], Praveen Sunareni[5], Sheng Xia[5], Rong Li[5], Raphael Voituriez[6,7], Matthieu Piel[2,8,9] and Ana-Maria Lennon-Duménil[1,8,9]

Dendritic cell (DC) migration in peripheral tissues serves two main functions: antigen sampling by immature DCs, and chemokine-guided migration towards lymphatic vessels (LVs) on maturation. These migratory events determine the efficiency of the adaptive immune response. Their regulation by the core cell locomotion machinery has not been determined. Here, we show that the migration of immature DCs depends on two main actin pools: a RhoA–mDia1-dependent actin pool located at their rear, which facilitates forward locomotion; and a Cdc42–Arp2/3-dependent actin pool present at their front, which limits migration but promotes antigen capture. Following TLR4–MyD88-induced maturation, Arp2/3-dependent actin enrichment at the cell front is markedly reduced. Consequently, mature DCs switch to a faster and more persistent mDia1-dependent locomotion mode that facilitates chemotactic migration to LVs and lymph nodes. Thus, the differential use of actin-nucleating machineries optimizes the migration of immature and mature DCs according to their specific function.

The activation of T lymphocytes depends on the capacity of dendritic cells (DCs) to internalize antigens at the site of infection and transport them to lymph nodes (LNs) as processed major histocompatibility complex–peptide complexes[1]. Sampling of peripheral tissues by immature DCs relies on their intrinsic antigen internalization capacity that includes both phagocytosis and macropinocytosis[2–4]. Tissue patrolling might also involve active DC locomotion as immature DCs have been shown to be motile in peripheral locations such as the mouse ear and gut[5,6]. On sensing of microbial stimuli, DCs acquire a mature phenotype that is associated with the Cdc42-dependent downregulation of macropinocytosis and the upregulation of co-stimulatory molecules for productive interaction with T lymphocytes[2,3,7]. Mature DCs also upregulate the chemokine receptor CCR7 at their surface[8], which allows them to respond to gradients of CCL21 secreted by the lymphatic endothelium, inducing their directional migration towards lymphatic vessels (LVs) and LNs (refs 9, 10). Extracellular molecules from the endothelium such as podoplanin were also shown to influence mature DC locomotion *in vivo*[11]. However, whether and how the core migration machinery of DCs is modified on innate sensing and impacts on their immune function remains unknown.

The mechanisms that enable cell migration have been extensively studied in adhesive cells moving on flat two-dimensional (2D) surfaces. In most cases, they involve cycles of cell front extension mediated by Arp2/3-dependent nucleation of branched filamentous actin, followed by cell rear retraction[12]. However, 2D migration rarely applies to immune cells, which mainly migrate in complex 3D environments *in vivo*. Although 3D environments are diverse in terms of molecular composition and geometry, they share a common property that does not apply to flat surfaces: cell confinement. Noticeably, DC locomotion was shown to be independent of integrin-mediated adhesion in 3D and 2D confined environments as well as *in vivo*[13–15], stressing the need to use experimental systems exhibiting the proper geometry to tackle the mechanisms underlying DC migration.

We used confining devices to investigate how sensing of microbial components regulates the intrinsic migratory capacity of DCs. We found that maturation of DCs in response to Toll-like receptor (TLR) 4–MyD88 signalling increases their migration speed and persistence by regulating actin-nucleation machineries. We further show that this cell-intrinsic change in DC motility is required for them to efficiently follow chemotactic gradients and reach LNs *in vivo*. We propose

[1]Inserm U932, Institut Curie, 12 rue Lhomond, 75005 Paris, France. [2]CNRS UMR144, Institut Curie, 12 rue Lhomond, 75005 Paris, France. [3]Institute for Immunology, Ludwig-Maximilian University of Munich, 80336 Munich, Germany. [4]Van Andel Research Institute, 333 Bostwick Avenue N.E., Grand Rapids, Michigan 49503, USA. [5]Johns Hopkins University School of Medicine, 855 N. Wolfe Street, Baltimore, Maryland 21205, USA. [6]CNRS UMR 7600, Université Pierre et Marie Curie, 4 Place Jussieu, 75005 Paris, France. [7]CNRS FRE 3231, Université Pierre et Marie Curie, 4 Place Jussieu, 75005 Paris, France. [8]These authors contributed equally to this work.
[9]Correspondence should be addressed to P.V., M.P. or A.-M.L.-D. (e-mail: pablo.vargas@curie.fr or mpiel@curie.fr or amlennon@curie.fr)

Received 11 December 2014; accepted 9 November 2015; published online 7 December 2015; DOI: 10.1038/ncb3284

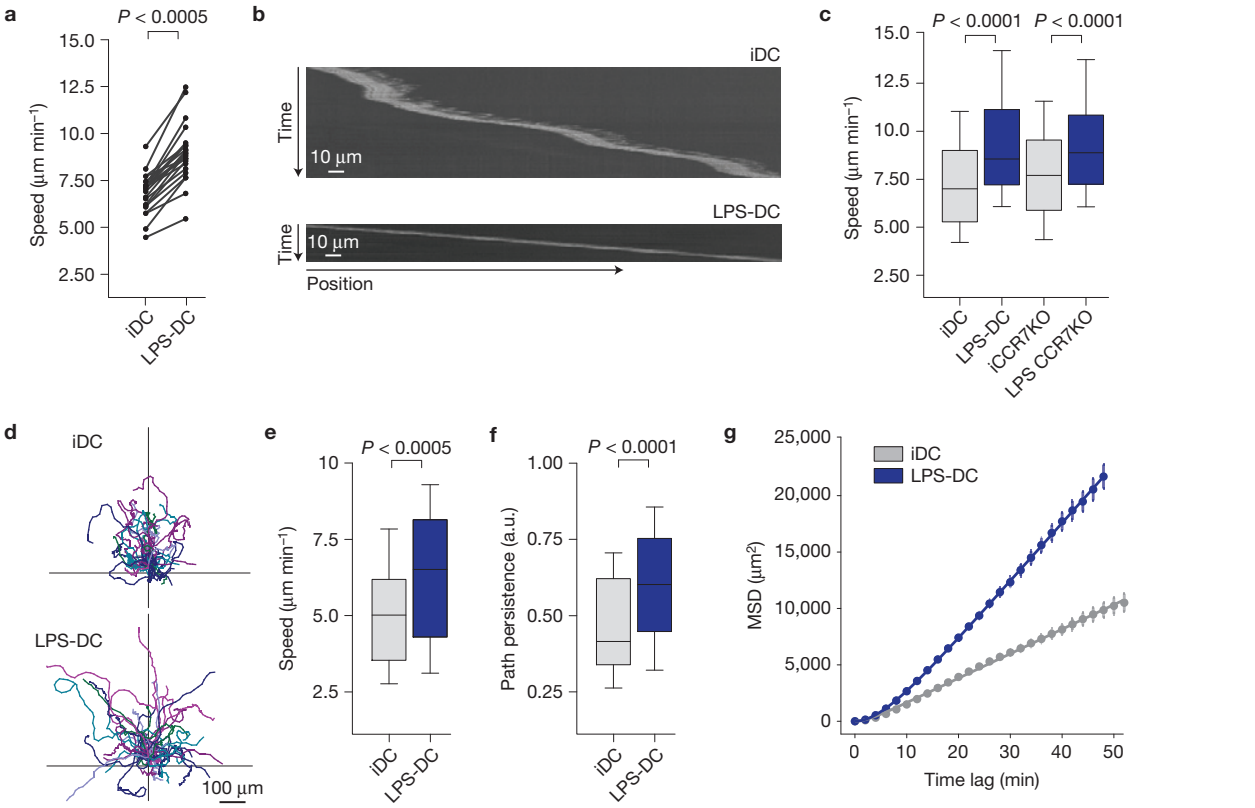

Figure 1 LPS activation induces fast and persistent DC migration. (**a**–**c**) Analysis of BMDCs migrating in 4 μm × 5 μm fibronectin-coated micro-channels. Cells were imaged between 6 and 16 h after LPS treatment (100 ng ml^{-1} for 30 min). (**a**) Mean instantaneous cell speed. Each dot represents the mean of one experiment (n = 29 experiments, >40 cells in each experiment). (**b**) Kymograph representative of an iDC and an LPS-DC migrating in micro-channels. (**c**) Analysis of CCR7KO DC migration in micro-channels (n = 150, 99, 145 and 151 cells for iDC, LPS-DC, iCCR7KO and LPS CCR7KO respectively). One representative experiment out of two is shown. (**d**–**g**) Analysis of DC migration under agarose. (**d**) Cell tracks of DCs migrating under agarose. Cells were imaged for 200 min. The starting point of each trajectory was translated to the origin of the plot. One representative experiment out of three is shown. (**e**,**f**) Mean instantaneous speed and path persistence of data depicted in **d** (n = 63 and 76 cells for iDC and LPS-DC respectively). (**g**) Mean square displacement (MSD) obtained from the data depicted in **d**. The Mann–Whitney test was applied for statistical analysis. In the box plots of **c**,**e**,**f** the bars include 90% of the points, the centre corresponds to the median and the box contains 75% of the data.

that regulation of the core cell migration machinery helps adapt the migratory behaviour of immature and mature DCs to their distinct functional requirements: environment sampling and antigen uptake for immature DCs and efficient migration to lymphoid organs for mature DCs.

RESULTS

Innate sensing induces fast and persistent DC migration

We asked whether innate sensing triggers cell-intrinsic changes in DC motility. To address this question, we compared the migration of immature DCs (iDCs) and LPS-treated mature DCs (LPS-DCs) in 1D confined micro-channels[15–17]. DCs pulsed with LPS for 30 min showed a significant increase in their migration speed after 6 h (Fig. 1a,b). This transient LPS treatment was sufficient to induce full DC maturation (Supplementary Fig. 1a,b). The increment in DC velocity was also observed in CCR7 knockout (KO) and pertussis toxin-treated cells (Fig. 1c and Supplementary Fig. 1c,d), excluding a role of G protein-coupled chemokine receptors. In contrast, both the LPS receptor TLR4 and its adaptor MyD88 (ref. 18) were needed for DC speed increment (Supplementary Fig. 1e,f). Hence, sensing of LPS triggers a TLR4–MyD88-dependent signalling cascade that promotes fast DC motility in 1D confined environments.

The trajectories of LPS-DCs were more continuous than those of iDCs, suggesting a more persistent locomotion mode (Fig. 1b). To measure cell migration persistence, we used the previously described 'under-agarose motility assay'[19], in which DCs are confined but freely move in two dimensions. LPS-DCs exhibited more directed trajectories as compared with iDCs (Fig. 1d). Accordingly, both their migration speed and path persistence were increased (Fig. 1e,f). As a consequence of that, LPS-DCs were more efficient in space exploration, as illustrated by their increased mean square displacement (Fig. 1g). Thus, TLR4 engagement triggers a cell-intrinsic response that results in mature DCs moving over larger distances as compared with their immature counterparts.

Innate sensing modifies actin dynamics in migrating DCs

We next investigated whether the impact of innate sensing on DC locomotion was associated with changes in their actin cytoskeleton. We have previously shown that iDCs alternate fast and slow motility phases when migrating in micro-channels[15]. Analysis of F-actin dynamics using DCs derived from LifeAct–GFP transgenic

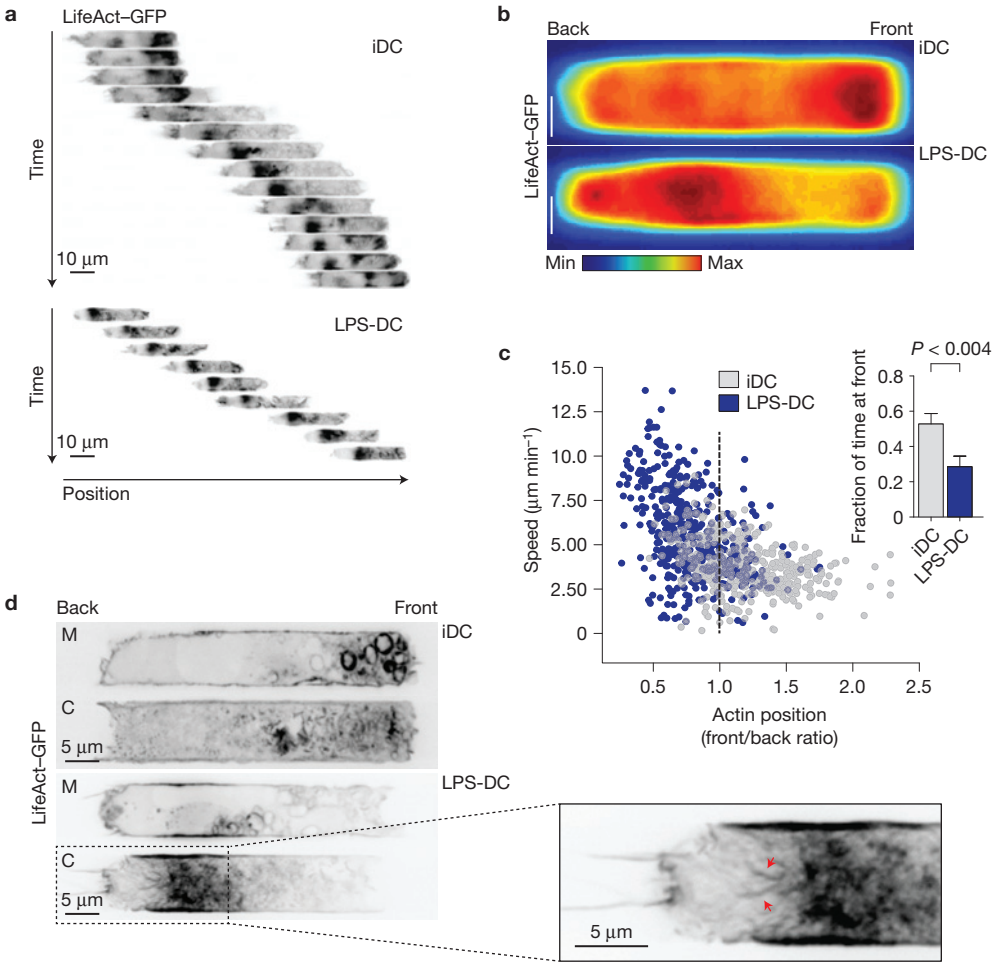

Figure 2 LPS activation of DCs modifies the dynamics of their actin cytoskeleton. (**a**–**d**) LifeAct–GFP imaging of BMDCs migrating in 8 μm × 5 μm fibronectin-coated micro-channels. (**a**) Sequential images of LifeAct–GFP DCs acquired on an epifluorescence microscope every 1 min with a ×20 objective. (**b**) LifeAct–GFP density maps. Scale bars, 2.5 μm. The signal recorded at each time point was integrated into a single image for single migrating cells (see Supplementary Fig. 2). The mean intensity obtained for each cell was then averaged into a single density map ($n = 31$ and 27 cells for iDC and LPS-DC respectively). One representative experiment out of four is shown. (**c**) Correlation between the LifeAct–GFP front/back ratio and instantaneous speed values from DCs migrating in micro-channels. Values were obtained from data shown in **b**. The inset shows the mean fraction of time spent by DCs with LifeAct–GFP concentrated at their front (first third of the cell). The Mann–Whitney test was applied for statistical analysis. Graphic shows mean and error bars correspond to s.e.m. (**d**) LifeAct–GFP DCs migrating in micro-channels and time lapsed on a spinning-disc microscope (×100). Middle (M) and cortical (C) planes were imaged. The red arrows on the zoomed image show actin cables formed at the rear of LPS-DC.

mice highlighted that iDCs concentrated F-actin at the cell front, particularly during phases of slow motion (Fig. 2a, upper panel). In contrast, the predominant F-actin pool of LPS-DCs was localized at the cell back. This pool of F-actin was also observed during phases of fast locomotion in iDCs (Fig. 2a, lower panel). These results were confirmed by quantifying the mean behaviour of the entire DC population using LifeAct–GFP density maps (Fig. 2b and Supplementary Fig. 2). Dynamic analysis showed that the presence of F-actin at the cell front inversely correlated with cell speed in both types of DC (Fig. 2c). However, iDCs spent significantly more time with actin at their front (Fig. 2c, inset). Noticeably, the predominant F-actin pool observed at the front of iDCs was mainly observed in ruffles and around macropinosomes[20] (Fig. 2d and Supplementary Videos 1 and 2). In contrast, the main F-actin structure present at the back of LPS-DCs localized at the cell cortex and included numerous actin cables (arrows in Fig. 2d and Supplementary Videos 1 and 3). Such cables were also occasionally observed in iDCs, in agreement with these cells exhibiting both slow and fast migration phases. These data highlight the existence of two main pools of F-actin in DCs: one at the cell front associated with slow motility, which is mainly observed in iDCs, and one at the cell back that correlates with fast migration.

F-actin at the front of iDCs depends on Arp2/3, limits migration but promotes antigen uptake

We next searched for the actin nucleators involved in the generation of these different actin pools. Branched actin nucleated by the Arp2/3 complex is known to promote migration by driving protrusion at the leading edge[21–23]. Arp2/3 has also been associated with membranes ruffling during macropinocytosis[24]. We therefore reasoned that Arp2/3 was needed for F-actin accumulation at the front of iDCs. Inhibiting Arp2/3 with CK666 (ref. 25) decreased the fraction of time iDCs spent with F-actin concentrated at their front (Fig. 3a,b). The

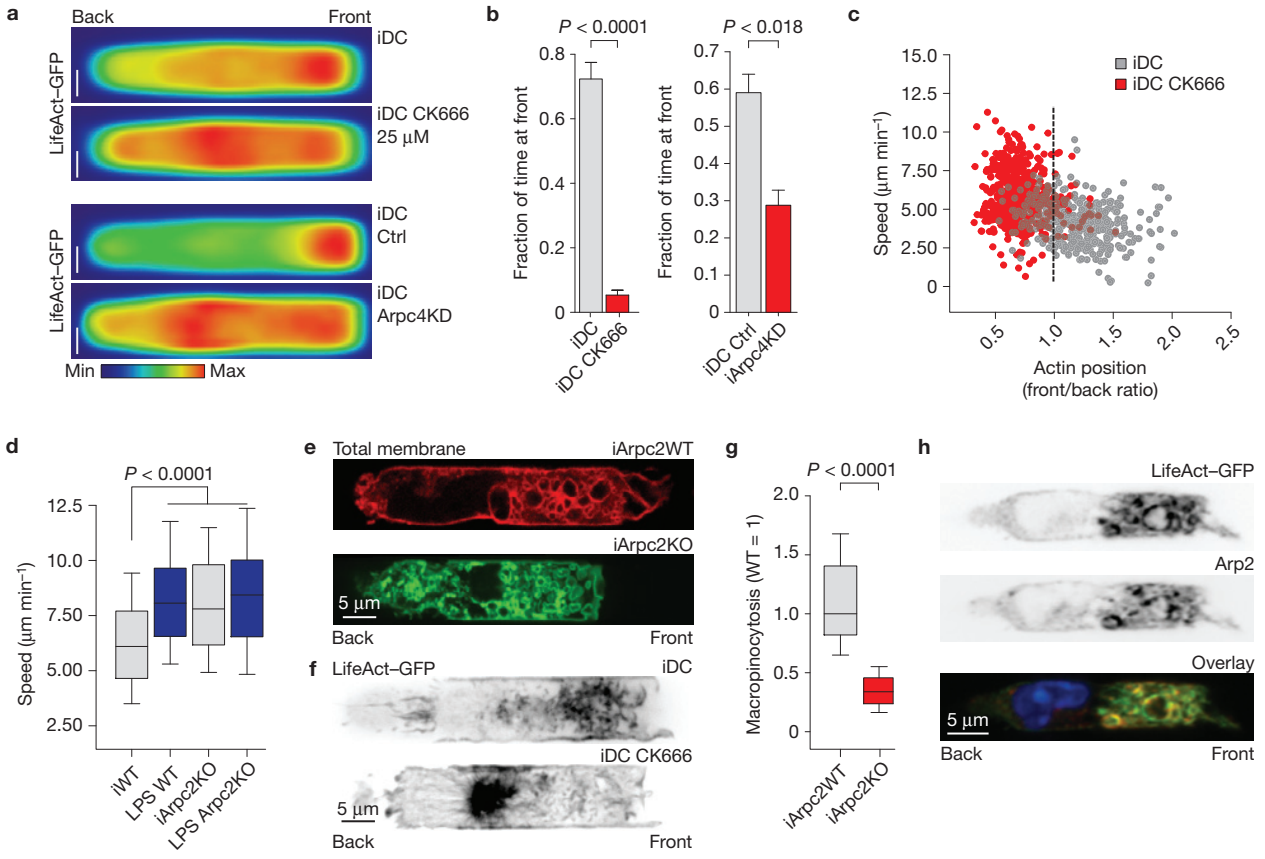

Figure 3 Arp2/3-dependent actin at the front of iDCs limits migration but promotes antigen uptake. (**a**) Mean LifeAct–GFP distribution in iDCs migrating in micro-channels and treated with the Arp2/3 inhibitor CK666 (25 μM) or silenced for Arpc4 ($n = 27$, 42, 28 and 26 cells for iDC, iDC CK666, iDC Ctrl and iArpc4KD respectively). Scale bars, 2.5 μm. One representative experiment out of three is shown. Internal controls are systematically used. (**b**) Dynamic analysis of the fraction of time spent by cells with LifeAct–GFP at their front obtained from data in **a**. Graphic shows mean and error bars correspond to s.e.m. (**c**) Correlation between the LifeAct–GFP front/back ratio and instantaneous speed values from DCs migrating in micro-channels obtained from data shown in **a**. (**d**) Mean instantaneous speed of WT or tamoxifen-induced Arpc2KO DCs migrating in micro-channels ($n = 308$, 255, 284 and 209 cells for iWT, LPS WT, iArpc2KO and LPS Arpc2KO respectively). One representative experiment out of three is shown. (**e**) Spinning-disc images (×100) of Arpc2 WT (TomatoFP$^+$) or KO (GFP$^+$) iDCs migrating in micro-channels. (**f**) Cortical LifeAct–GFP signal of control or CK666-treated iDCs migrating in micro-channels. (**g**) Quantification of fluorescent ovalbumin uptake in iDCs derived from WT and tamoxifen-induced Arpc2KO DCs migrating in micro-channels ($n = 36$ and 37 cells for Arpc2WT and Arpc2KO respectively). One representative experiment out of two is shown. (**h**) Immunofluorescence analysis of Arp2 in iDCs migrating in micro-channels analysed using a spinning-disc microscope (×100). The overlay shows LifeAct–GFP (green), Arp2 immunoreactivity (red) and DAPI staining (blue).The Mann–Whitney test was applied for all statistical analyses. In the box plots of **d** and **g** the bars include 90% of the points, the centre corresponds to the median and the box contains 75% of the data.

same result was observed when using siRNA targeting Arpc4, one of the actin-binding subunits of the Arp2/3 complex[26] (Fig. 3a,b and Supplementary Fig. 3a). Strikingly, high-resolution imaging showed that CK666 treatment led to the accumulation of cortical actin filaments at the rear of iDCs (Fig. 3f), which were organized in a similar structure to the one observed in LPS-DCs. None of these treatments significantly affected LifeAct–GFP distribution in LPS-DCs, showing that F-actin concentrates at their back independently of Arp2/3 (Supplementary Fig. 3b,c). Changes in F-actin distribution were not due to DC maturation induced by Arp2/3 inhibition (Supplementary Fig. 3d). Hence, Arp2/3 is required to maintain the pool of F-actin at the front of iDCs but is dispensable for F-actin enrichment at the rear of LPS-DCs.

Strikingly, Arp2/3 inhibition in iDCs not only decreased the accumulation of F-actin at their front but also increased their speed (Fig. 3c and Supplementary Fig. 3e). Although unexpected, this result is consistent with LPS-DCs lacking Arp2/3-dependent actin at the cell front and migrating faster than iDCs. A similar increase in cell velocity was observed in conditional Arpc2KO iDCs, which migrated as fast as LPS-DCs (Fig. 3d and Supplementary Fig. 3f). The speed of Arpc2KO DCs was also significantly increased in under-agarose migration assays (Supplementary Fig. 3g). This was independent of DC maturation (Supplementary Fig. 3h). Thus, unlike protrusion-based locomotion[21–23], the Arp2/3-dependent pool of F-actin present at the front of iDCs limits their migration.

Noticeably, the front of Arpc2KO iDCs contained small vesicles instead of large macropinosomes (Fig. 3e and Supplementary Fig. 3i), indicating that Arp2/3-dependent F-actin might be rather required for antigen macropinocytosis than for iDC locomotion. Accordingly, the amount of extracellular fluid enclosed in these vesicles was diminished when Arp2/3 was inhibited or knocked out (Fig. 3g and Supplementary Fig. 3j). Antigen uptake was also decreased

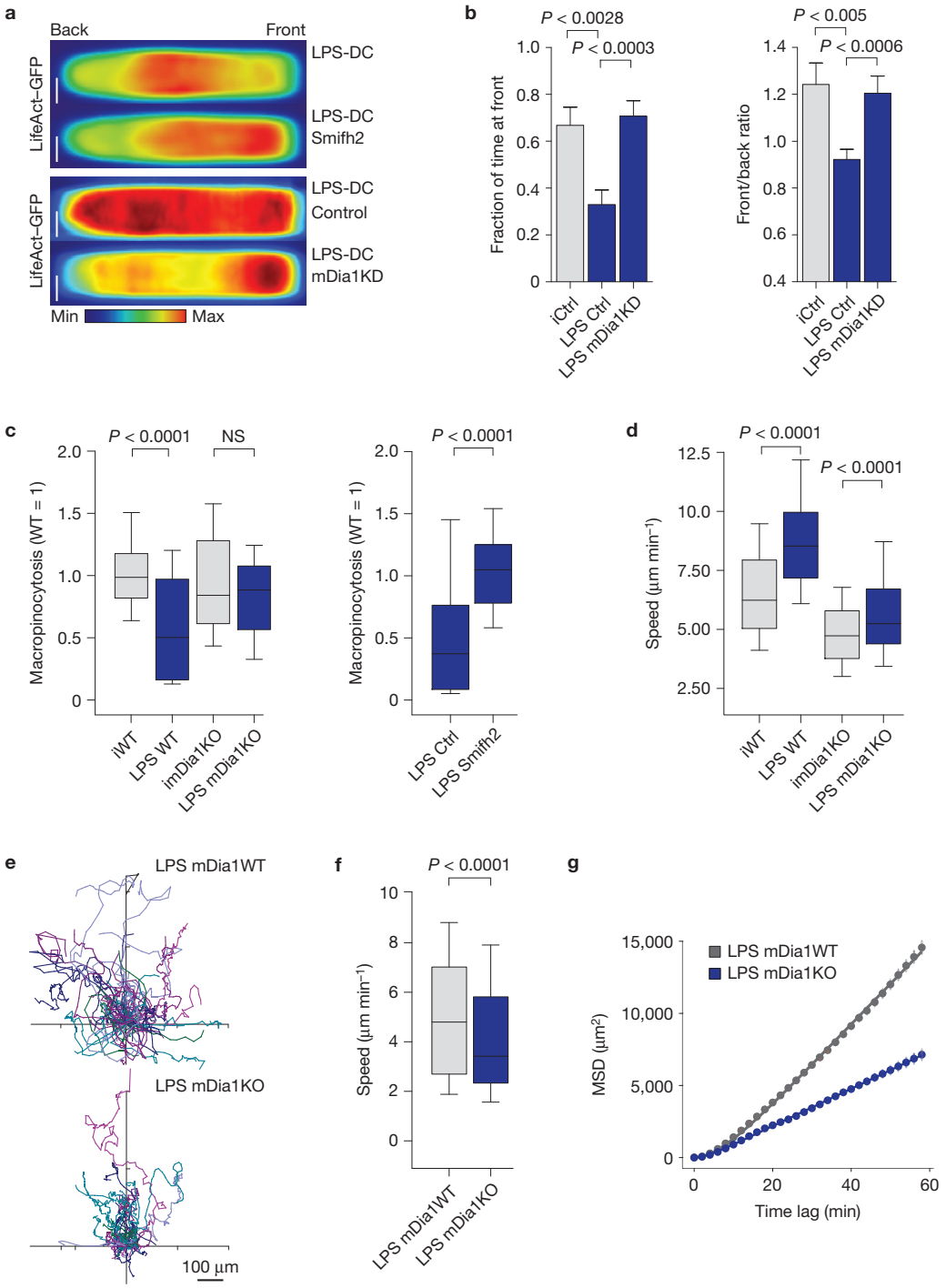

Figure 4 mDia1 is required for fast DC migration. (**a**,**b**) Analysis of DC migration in micro-channels. (**a**) Mean LifeAct–GFP distribution obtained from LPS-DCs migrating in micro-channels and treated with the formin inhibitor Smifh2 (25 µM) or silenced for mDia1. One representative experiment out of three is shown. Scale bars, 2.5 µm. (**b**) Dynamic analysis of the fraction of time spent by cells with LifeAct–GFP at their front obtained from data shown in **a** ($n = 21$, 22 and 31 for iCtrl, LPS Ctrl and LPS mDia1KD respectively). Graphic shows mean and error bars correspond to s.e.m. (**c**) Quantification of fluorescent ovalbumin uptake in DCs derived from WT and mDia1KO mice or treated with Smifh2 (25 µM) while migrating in micro-channels ($n = 33$, 36, 38, 45, 23 and 28 cells for WT, LPS DC, imDia1KO, LPS mDia1KO, LPS Ctrl and LPS Smifh2 respectively). One representative experiment out of two is shown. NS, not significant. (**d**) Mean instantaneous speed of control and mDia1KO DCs migrating in micro-channels ($n = 272$, 218, 192 and 310 cells for iWT, LPS WT, imDia1KO and LPS mDia1KO respectively). One representative experiment out of three is shown. (**e**–**g**) Analysis of DC migration under agarose. (**e**) Cell tracks of WT and mDia1KO LPS-DCs. Cells were imaged for 200 min. The starting point of each trajectory was translated to the origin of the plot. $n = 129$ and 69 cells for LPS mDia1WT and LPS mDia1KO respectively. One representative experiment out of three is shown. (**f**) Mean instantaneous speed obtained from data shown in **d**. (**g**) Mean square displacement (MSD) quantified from the data depicted in **e**. The Mann–Whitney test was applied for all statistical analyses. In the box plots of **c**,**d** and **f** the bars include 90% of the points, the centre corresponds to the median and the box contains 75% of the data.

in LPS-DCs, consistent with less actin accumulating at their front (Supplementary Fig. 3k). Immunofluorescence analysis showed that Arp2/3 was indeed enriched around macropinosomes at the front of iDCs (Fig. 3h). Density maps obtained from fixed cells highlighted that Arp2/3 exhibited a similar distribution in iDCs and LPS-DCs (Supplementary Fig. 3l). This observation suggests that the accumulation of F-actin at the back of LPS-DCs does not result from changes in Arp2/3 distribution. Together, our data indicate that antigen uptake—but not DC migration—requires Arp2/3.

mDia1-dependent actin nucleation at the cell rear controls fast DC migration

Arp2/3 inhibition or silencing had no major impact on actin distribution and migration of LPS-DCs, suggesting that the actin cables observed at their back result from alternative nucleating factors. We therefore investigated the possible involvement of formins, which nucleate non-branched actin filaments[27–29]. The broad formin inhibitor Smifh2 (ref. 30) induced the redistribution of actin from the back to the front of both iDCs and LPS-DCs (Fig. 4a and Supplementary Fig. 4a). This indicates that formin activity maintains F-actin at the DC rear. Among the 15 members of the formin family, mDia1 is known to be required for T-cell[31,32] and DC (ref. 33) migration from peripheral tissues to LNs. In addition, mDia1 is the main formin involved in nucleation of the bulk actin cortex[34]. Accordingly, analysis by immunofluorescence of mDia1 intracellular distribution showed that it was present all along the cortex in LPS-DCs (Supplementary Fig. 4b). As mDia1 staining required cell fixation with methanol, which did not preserve the predominant F-actin structure observed at the back of LPS-DCs, we could not observe whether mDia1 localized to it. Nonetheless, density maps showed that mDia1 localization followed F-actin distribution: whereas mDia1 was enriched at the front of iDCs, it increased at the back of LPS-DCs (Supplementary Fig. 4c). We therefore evaluated the specific contribution of mDia1 to LifeAct–GFP dynamics in migrating DCs. The pool of F-actin present at the rear of LPS-DCs was significantly reduced when silencing mDia1 (Fig. 4a and Supplementary Fig. 4d). In addition, the time spent by mDia1-silenced cells with F-actin concentrated at their front and their front/back F-actin ratio were increased (Fig. 4b). The effect of mDia1 was comparable to the one of Smifh2, suggesting that it is indeed the main formin involved. Of note, macropinocytosis was restored to levels comparable to the ones of iDCs in both mDia1KO and Smifh2-treated LPS-DCs, in agreement with F-actin accumulating at their front (Fig. 4c).

Knocking out the mDia1 gene[35] or inhibiting formins with Smifh2 reduced the migration speed and persistence of both iDCs and LPS-DCs (Fig. 4d and Supplementary Fig. 4e,f). However, the impact of mDia1 deficiency on cell speed was stronger in LPS-DCs. This result suggests that mDia1 is needed for fast DC migration and has therefore a greater impact on the speed of LPS-DCs, which predominantly migrate fast, than on iDCs, which alternate between fast and slow motility phases. Accordingly, we found that the highest speed reached by iDCs and LPS-DCs was significantly diminished in the absence of mDia1 (Supplementary Fig. 4g). In addition, under-agarose migration assays showed that mDia1-deficient LPS-DCs were slower and less efficient in space exploration as compared with wild-type cells (Fig. 4e–g). The migration defect of mDia1KO DCs was not due to impaired maturation (Supplementary Fig. 4h). Hence, unlike Arp2/3, mDia1 controls the maintenance of F-actin at the back of fast-moving DCs and is required for their persistent locomotion. Of note, inhibition of Arp2/3 in mDia1KO DCs had no effect on their migratory phenotype (Supplementary Fig. 4i). Thus, iDCs exhibit an mDia1-dependent F-actin pool at their rear needed for fast migration and an Arp2/3-dependent F-actin pool at their front that limits locomotion but is required for antigen uptake. In contrast, LPS-DCs predominantly exhibit mDia1-dependent F-actin at their back and therefore migrate faster and more persistently but do not efficiently take up extracellular material.

Actin nucleation at the front and back of DCs respectively relies on Cdc42 and RhoA

Our data show that inhibiting or knocking out Arp2/3 in iDCs is sufficient to recapitulate the phenotype of mature LPS-DCs in terms of migration and macropinocytosis, suggesting that LPS-induced DC maturation leads to the downregulation of Arp2/3 expression or activity. However, no change in the expression levels of Arp2/3 was observed on LPS treatment of DCs (Supplementary Figs 5a,b and 8a), implying that its actin-nucleation activity might rather be diminished in mature DCs. Downregulation of the small GTPase Cdc42, which activates Arp2/3 through the nucleation-promoting factor WASP (ref. 36), was shown to be responsible for reduced macropinocytosis in LPS-DCs (ref. 2). We therefore reasoned that down-modulation of Cdc42 activity might lead to reduced Arp2/3 activation and fast migration in mature DCs. To address this question, we used DCs generated from conditional Cdc42KO mice[37] or the Cdc42 inhibitor ML141. Cdc42KO and ML141-treated iDCs exhibited the same phenotype as Arp2/3-deficient DCs: they migrated as fast as LPS-DCs and spent less time with F-actin concentrated at their front (Fig. 5a–c and Supplementary Fig. 5c). As observed when inhibiting Arp2/3, inhibition of Cdc42 activity markedly decreased macropinocytosis in iDCs (Fig. 5d). No major effect of Cdc42 deficiency/inhibition was observed on F-actin distribution and migration of LPS-DCs (Fig. 5b,c). In sharp contrast, RhoAKO or RhoA-inhibited DCs exhibited a phenotype similar to the one of mDia1KO cells: their speed was decreased and, when treated with LPS, they accumulated F-actin at their front and internalized extracellular material by macropinocytosis (Fig. 5e–h). DC maturation was unaffected by both Cdc42 and RhoA deficiencies (Supplementary Fig. 5d). Therefore, downregulation of Cdc42 activity in mature LPS-DCs leads to decreased Arp2/3-mediated actin nucleation and macropinocytosis at their front. As a result of this, they adopt a fast migratory phenotype that relies on RhoA–mDia1-dependent actin nucleation.

mDia1 is required for chemotactic migration of mature DCs

In vivo, DCs increase their persistence when attracted to CCL21 gradients[10] on LVs. We therefore asked whether the mDia1-dependent migration increment observed in LPS-DCs affected their chemotactic migration (Supplementary Fig. 6a). Using collagen gels[13], we found that LPS-DCs but not iDCs—which do not express CCR7—migrated towards the CCL21 source (Supplementary Fig. 6b and Supplementary Video 4). Both, control and mDia1KO LPS-DCs expressed similar levels of surface CCR7 (Supplementary Fig. 6c) and sensed the direction of the gradient with similar efficiencies as shown by

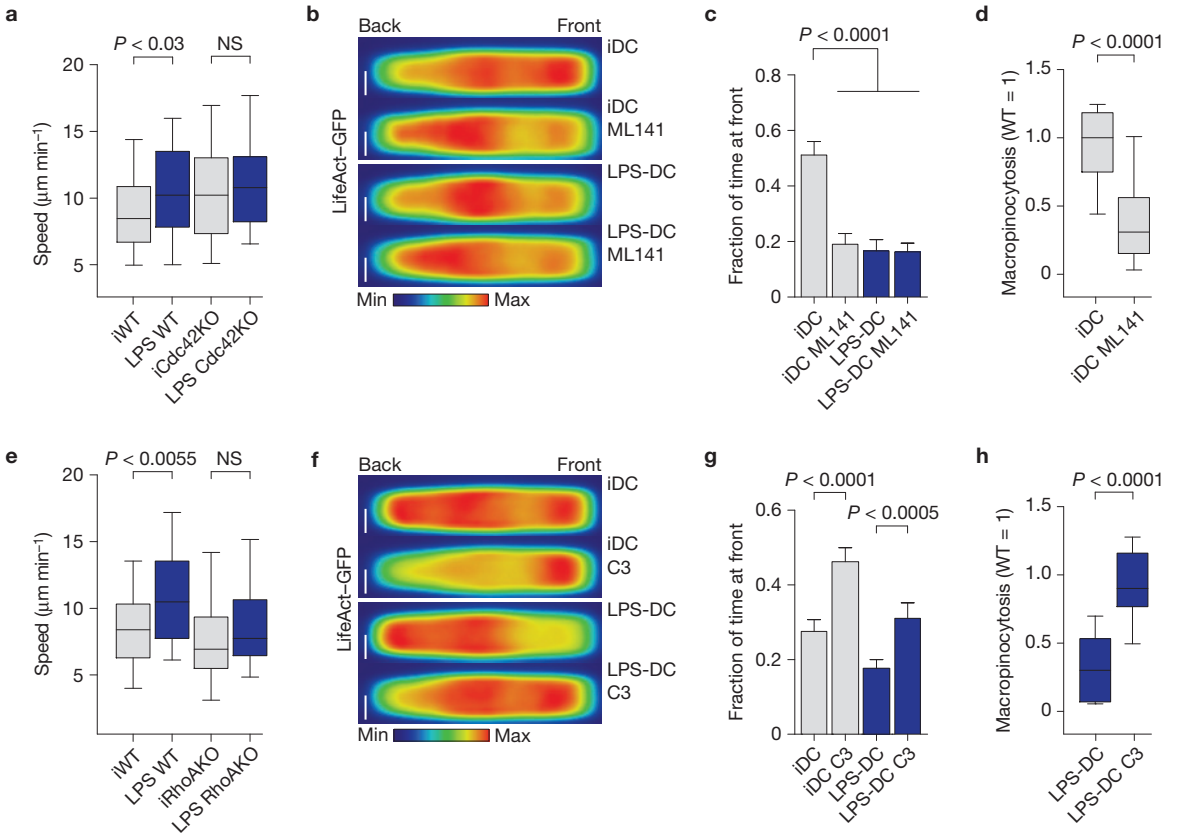

Figure 5 Cdc42 and RhoA respectively control the migration of iDCs and LPS-DCs. (**a**) Mean instantaneous speed of Cdc42WT and KO DCs migrating in micro-channels ($n = 111$, 33, 129 and 110 cells for iWT, LPS WT, iCdc42KO and LPS Cdc42KO respectively). One representative experiment out of two is shown. NS, not significant. (**b**) Mean LifeAct–GFP distribution in DCs treated with the Cdc42 inhibitor ML141 (50 μM) ($n = 25$, 32, 33 and 33 cells for iDC, iDC ML141, LPS-DC and LPS-DC ML141 respectively). One representative experiment out of two is shown. Scale bars, 2.5 μm. (**c**) Dynamic analysis of the fraction of time spent by cells with LifeAct–GFP at their front obtained from data in **b**. Graphic shows mean and error bars correspond to s.e.m. (**d**) Quantification of fluorescent ovalbumin uptake in iDCs treated with ML141 (50 μM) while migrating in micro-channels ($n = 15$ and 29 cells for iDC and iDC ML141 respectively). One representative experiment out of two is shown. (**e**) Mean instantaneous speed of WT and RhoAKO DCs migrating in micro-channels ($n = 86$, 102, 45 and 109 cells for iWT, LPS-DC, iRhoAKO and LPS RhoAKO respectively). One representative experiment out of two is shown. NS, not significant. (**f**) Mean LifeAct–GFP distribution in DCs migrating in micro-channels and treated with the RhoA inhibitor C3 convertase (1 μg ml^{-1}) ($n = 42$, 97, 34 and 59 cells for iDC, iDC C3, LPS-DC and LPS-DC C3 respectively). One representative experiment out of two is shown. Scale bars, 2.5 μm. (**g**) Dynamic analysis of the fraction of time spent by cells with LifeAct–GFP at their front obtained from data shown in **f**. Graphic shows mean and error bars correspond to s.e.m. (**h**) Quantification of fluorescent ovalbumin uptake in iDCs treated with C3 convertase (1 μg ml^{-1}) while migrating in micro-channels ($n = 23$ and 28 cells for LPS-DC and LPS-DC C3 respectively). One representative experiment out of two is shown. The Mann–Whitney test was applied for all statistical analyses. In the box plots of **a**,**d**,**e** and **h** the bars include 90% of the points, the centre corresponds to the median and the box contains 75% of the data.

the distribution of their trajectories (Fig. 6a,b and Supplementary Video 5). However, individual cell tracks were shorter in mDia1KO LPS-DCs (Fig. 6b). Further analysis highlighted that wild-type LPS-DCs increased both their speed and persistence while approaching the chemokine source (Fig. 6c,d and Supplementary Fig. 6b). No such increase was observed in the absence of chemokine (Fig. 6e). This process referred to as orthotaxis has been proposed as a mechanism by which chemokine gradients increase the efficiency of directional migration[38]. Strikingly, orthotaxis was impaired in mDia1KO LPS-DCs (Fig. 6c,d and Supplementary Fig. 7a–c). Hence, mDia1 not only increases the speed of LPS-DCs but is further required for their chemotactic migration, suggesting that the increment of DC migration induced on LPS sensing impacts chemokine-driven locomotion.

We found that Arp2/3 inhibition had no impact on directionality, speed or persistence of LPS-DCs migrating in CCL21 gradients (Fig. 6f,g), consistent with our result showing that LPS-DCs are insensitive to Arp2/3 inhibition in terms of F-actin distribution and migration speed. We conclude that mDia1 but not Arp2/3 controls the chemotactic movement of LPS-DCs in collagen gels. Surprisingly, none of them affected directionality, suggesting that alternative mechanisms might account for the regulation of cell orientation along CCL21 gradients.

mDia1 is required for arrival of LPS-DCs to lymphatic vessels and lymph nodes

So far, we have shown that mDia1 plays a key role in the TLR4–MyD88-dependent transition from slow to fast and persistent DC locomotion and is required for their chemotaxis *in vitro*. To evaluate whether this equally applies in tissues, we analysed the migration of LPS-DCs towards LVs in explanted ear epidermal

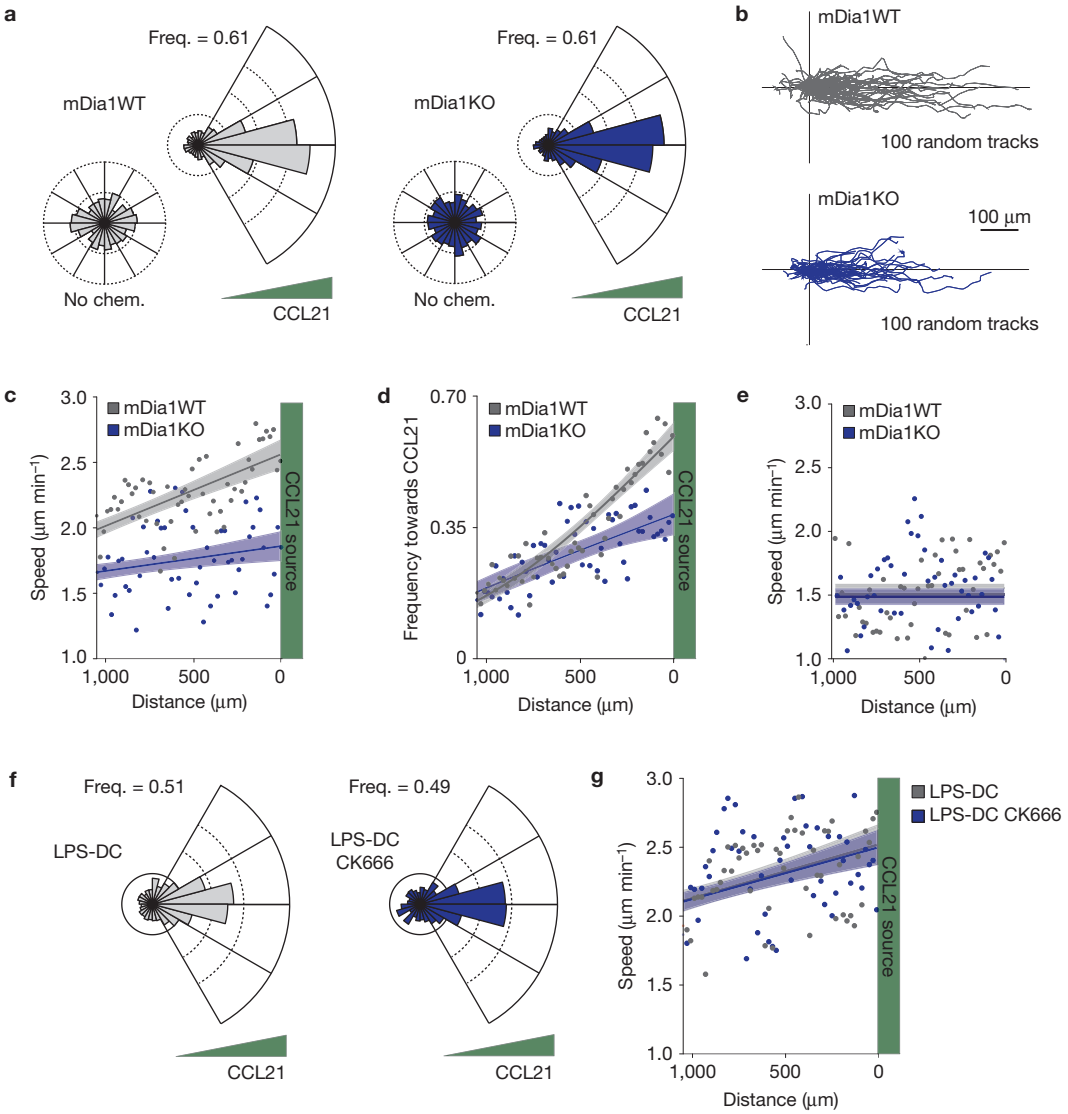

Figure 6 mDia1 is required for the chemotactic response of mature DCs. (**a**–**g**) Chemotactic response of LPS-DCs embedded in a collagen gel containing a CCL21 gradient. Frequency (Freq.) was calculated in 500 random tracks because of oversampling. One representative experiment out of three is shown. (**a**) Directionality of trajectories during the chemotactic response or in the absence of chemokines (No chem.) of mDia1WT and mDia1KO LPS-DCs. (**b**) One hundred random tracks of LPS-DCs undergoing chemotaxis. (**c**) Mean speed of LPS-DCs represented as a function of the distance to the CCL21 source. (**d**) Frequency of movement of LPS-DCs in the direction of the gradient represented as a function of the distance to the CCL21 source. (**e**) Speed of LPS-DCs in the absence of CCL21. (**f**) Directionality of trajectories of LPS-DCs treated or not with CK666 (25 µM) during chemotactic response as in **a**. (**g**) Mean speed of CK666-treated LPS-DCs represented as a function of the distance to the CCL21 source. Trend lines with 95% confidence interval are shown in **c**,**d**,**e** and **g**.

sheets[39] (Supplementary Fig. 7d). mDia1KO mature DCs exhibited decreased motility as compared with wild-type LPS-DCs when moving in the same tissue (Fig. 7a,b). Consequently, their ability to explore the space was reduced as depicted by their diminished mean square displacement (Fig. 7c). Analysis of cell tracks showed that control LPS-DCs exhibited a persistent random walk migration mode biased towards LVs whereas mDia1KO cells followed an isotropic diffusive pattern of locomotion (Fig. 7c and Supplementary Fig. 7e). As observed in collagen gels, wild-type LPS-DCs increased their speed and directionality while approaching LVs (Fig. 7d,e). In contrast, mDia1KO LPS-DCs migrated randomly, did not exhibit any significant directional bias towards LVs (Fig. 7b–e) and barely reached these vessels (Fig. 7f). Migration of Arpc2KO LPS-DCs to LVs was not altered (Fig. 7g), in agreement with these cells exhibiting wild-type migratory and chemotactic phenotypes *in vitro*. Hence, mDia1 is required for orthotaxis of mature DCs *in vivo*.

The absence of mDia1 had a stronger impact on DC migration in the skin than in collagen gels, suggesting that a persistent random walk is particularly critical for DC migration along chemokine gradients in the complex geometry of tissues. Consistent with these results, we found that the arrival of mDia1KO LPS-DCs to LNs on transfer into the footpad of wild-type recipients was also significantly decreased[33] (Fig. 7h and Supplementary Fig. 7f). We conclude that mature DCs must harbour an mDia1-dependent fast and persistent migration

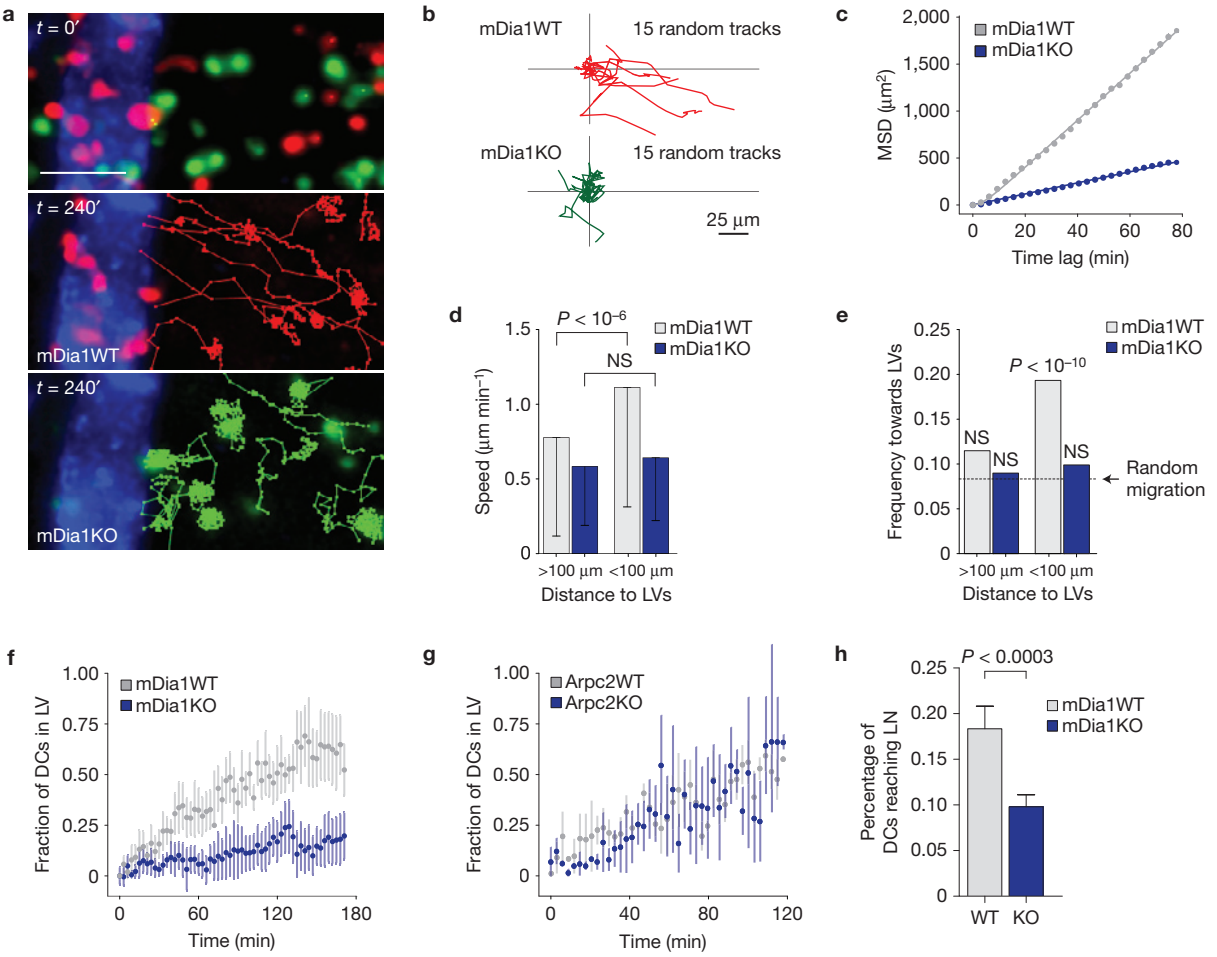

Figure 7 mDia1 is required for migration of mature DCs to LVs and LNs *in vivo*. (**a**–**f**) Migration of LPS-DCs in mouse ear explants ($n = 50$ and 59 cells for LPS mDia1WT and LPS mDia1KO respectively). Pool of three independent experiments. (**a**) Cell tracks from mDia1WT (red) or mDia1KO (green) LPS-DCs migrating in the proximity of LVs (stained with LYVE-1; blue) in a mouse epidermal ear sheet. Scale bar, 50 μm. (**b**) Fifteen randomly selected tracks of mDia1WT and mDia1KO LPS-DCs migrating in an epidermal ear sheet as shown in **a**. (**c**) Mean square displacement (MSD) of mDia1WT and mDia1KO LPS-DCs migrating in an epidermal ear sheet. The MSD curve of mDia1KO cells is fitted with a simple linear expression, reflecting the isotropic random walk-like behaviour of this population. Instead, the MSD curve of mDia1WT cells showed a first nonlinear increase followed by a linear dependency, as expected for biased persistent random walk and is fitted with Fürth's formula. (**d**) Mean instantaneous speed of LPS-DCs represented as a function of the distance to the closest LV. Error bars correspond to s.d. (**e**) Frequency of cell movements in the direction of the closest LV. Statistical analysis was performed comparing values with respect to random migration from data shown in **d**. Student's *t*-test and Pearson's χ^2 test were applied in **d** and **e**, respectively. NS, not significant. (**f**,**g**) Fraction of DCs that reach LVs plotted as a function of time. Error bars correspond to s.e.m. (**h**) *In vivo* migration of LPS-DCs to LNs. The number of mDia1WT and mDia1KO DCs that arrive at popliteal LNs after injection in the footpad was analysed by fluorescence-activated cell sorting after 16 h ($n = 9$ mice per condition pooled from three independent experiments). The Mann–Whitney test was applied for statistical analysis in **h**. Graphic shows mean and error bars correspond to s.e.m.

mode to follow chemotactic CCL21 gradients in peripheral tissues and reach LNs *in vivo*.

DISCUSSION

We here show that sensing of the microbial compound LPS increases the migration speed and persistence of DCs, a process required for efficient chemotaxis to LVs and homing to LNs. This relies on cell-intrinsic changes in F-actin distribution that result from the differential use of actin-nucleating machineries in immature and mature DCs. Thus, regulation of the core locomotion machinery on activation of the LPS–TLR4–MyD88 axis helps tune the migratory behaviour of immature and mature DCs according to their distinct functional requirements: environment sampling and antigen uptake for immature DCs and fast migration to LNs for mature DCs. Whether other microbial or inflammatory stimuli equally affect actin dynamics and chemotaxis of DCs shall now be addressed.

We found that Arp2/3 nucleates branched actin at the front of iDCs, which harbour a speed-fluctuating behaviour[15]. This F-actin pool compromised cell migration but promoted antigen capture by macropinocytosis. In mature LPS-DCs, which exhibited a poor macropinocytic capacity but migrated faster and more persistently than iDCs, F-actin was predominantly observed at the cell rear and relied on mDia1 and RhoA activities. Consistently, the levels of phosphorylated myosin II light chain, which are regulated by RhoA, were increased in LPS-DCs as compared with iDCs (Supplementary Figs 7g and 8b). These data suggest that mDia1-dependent actin

nucleation is used in both LPS-DCs and iDCs for locomotion, whereas Arp2/3-dependent actin nucleation is used by iDCs to integrate antigen uptake to cell migration. On LPS sensing, actin nucleation at the front by Arp2/3 is strongly reduced, allowing mature DCs to adopt a fast and directional migration mode. Strikingly, Cdc42, whose activity was shown to be downregulated after treatment of DCs with LPS (ref. 2), limited iDC migration but promoted macropinocytosis, as did Arp2/3. This result strongly suggests that Cdc42 inactivation is responsible for the loss of Arp2/3 activity in LPS-DCs.

Surprisingly, the presence of an Arp2/3-dependent F-actin pool at the front of iDCs reduced their motility. This result was unexpected given that Arp2/3 is described as promoting forward locomotion by generating protrusions at the cell front[21–23], showing that the branched actin network plays different roles in cell migration based on the environment geometry and the cell type. On 2D surfaces, cells exert forces parallel to the substratum owing to the presence of Arp2/3 at the cell front. In contrast, in confined environments, motility results from pushing forces exerted perpendicularly to the substratum[40]. Our data suggest that these forces are generated by formins and not by Arp2/3, consistent with findings made in HL-60 cells migrating in micro-channels[41]. Arp2/3 at the front of iDCs might impair migration by promoting the formation of macropinosomes, as suggested by results highlighting that migration and macropinocytosis are antagonistic in *Dictyostelium* and iDCs (refs 42,43). In iDCs, this antagonism results from the recruitment of myosin II to macropinosomes, which disrupts the back-to-front gradient of the motor protein and leads to speed reduction[42]. The present study therefore suggests that myosin II recruitment to the front of iDCs might rely on local Arp2/3 activity. Whether the presence of both mDia1 and Arp2/3 at the front of iDCs is needed to generate anti-polar actin filaments to which myosin II could bind should be explored.

We found that mature LPS-DCs must adopt an mDia1-dependent fast and persistent migration mode to efficiently migrate along CCL21 gradients. Of note, although Arp2/3 did not regulate chemotaxis of mature DCs, we cannot exclude that Arp2/3-dependent protrusion at the cell front is required for chemotaxis of iDCs. Remarkably, the impact of mDia1 deficiency on chemotaxis was more severe in epidermal ear sheets than in collagen gels. This was not due to impaired Clec2 expression in mDia1-deficient DCs (Supplementary Fig. 6b), a surface lectin that binds to podoplanin present on endothelial cells and is required for DC recruitment to LVs (ref. 11). This difference might rather result from the complex architecture of tissues that may locally modify the linearity of CCL21 gradients so that mature DCs must harbour a persistent random walk locomotion mode to not 'get distracted' and maintain their directionality. In that context, the presence of F-actin at the front of mDia1KO DCs could favour the sensing of such local gradient modifications, reducing their directional memory. Future experiments aimed at analysing the requirement for mDia1 in DCs migrating in irregular chemokine gradients *ex vivo* shall help address this hypothesis. □

METHODS

Methods and any associated references are available in the online version of the paper.

Note: Supplementary Information is available in the online version of the paper

ACKNOWLEDGEMENTS

The authors thank the PICT IBiSA platform at Institut Curie (CNRS UMR144, especially V. Fraisier) and the Institut Curie animal facility. P.V. thanks B. Goic for support, patience and critical reading of the manuscript. P.V. was supported by fellowships from Region Ile-de-France, Fondation pour la Recherche Médicale (FRM) and Institut Curie. M.B. and M.C. benefited from fellowships from Association pour la Recherche contre le Cancer and FRM respectively. S.M.K.-G. and A.S.A. were supported by the Grand Rapids Community and the Lunn Hope Foundations, the Van Andel Endowment, and the Purple Community. T.B. was supported by DFG SFB 1054-B03 and SFB 914-A06. This work was financially supported by grants from: the City of Paris, the European Research Council and the DCBIOL Labex (ANR-10-IDEX-0001-02-PSL* and ANR-11-LABX-0043) to A.-M.L.-D. (Strapacemi 243103) and the Association Nationale pour la Recherche (ANR-09-PIRI-0027-PCVI) and the InnaBiosanté foundation (Micemico) to A.-M.L.-D., M.P. and R.V.

AUTHOR CONTRIBUTIONS

P.V. designed, performed and analysed most experiments, prepared all manuscript figures and strongly participated in article writing and project conception. P.M. conceived and performed trajectory analyses and modelling. M.B. set up and assisted with siRNA-mediated silencing, qPCR and macropinocytosis experiments. P.J.S. and H.-R.T. assisted in optimizing micro-channel experiments. P.J.S. further helped P.V. with article revision. P.P. built the program for actin distribution analysis in migrating DCs. M.M. created all codes for quantification of macropinocytosis and arrival of DCs to LVs. M.C. carried out the initial observation of increased migration speed and decreased antigen uptake in CK666-treated iDCs. E.T. helped with micro-fabrication. D.L. assisted P.V. with immunofluorescence experiments. D.O. performed immunoblots. M.R. set up collagen gel experiments. T.B. generated and provided Cdc42 and RhoA conditional KO mice. S.M.K.-G. and A.S.A. generated and provided mDia1KO mice. S.X., P.S. and R.L. generated and provided Arpc2 conditional KO mice. R.V. conceived and performed migration modelling. M.P. and A.-M.L.-D. designed the overall research and wrote the manuscript.

COMPETING FINANCIAL INTERESTS

The authors declare no competing financial interests.

Published online at http://dx.doi.org/10.1038/ncb3284
Reprints and permissions information is available online at www.nature.com/reprints

1. Mellman, I. & Steinman, R. M. Dendritic cells: specialized and regulated antigen processing machines. *Cell* **106,** 255–258 (2001).
2. Garrett, W. S. *et al.* Developmental control of endocytosis in dendritic cells by Cdc42. *Cell* **102,** 325–334 (2000).
3. Cella, M., Sallusto, F. & Lanzavecchia, A. Origin, maturation and antigen presenting function of dendritic cells. *Curr. Opin. Immunol.* **9,** 10–16 (1997).
4. Sallusto, F., Cella, M., Danieli, C. & Lanzavecchia, A. Dendritic cells use macropinocytosis and the mannose receptor to concentrate macromolecules in the major histocompatibility complex class II compartment: downregulation by cytokines and bacterial products. *J. Exp. Med.* **182,** 389–400 (1995).
5. Farache, J. *et al.* Luminal bacteria recruit CD103+ dendritic cells into the intestinal epithelium to sample bacterial antigens for presentation. *Immunity* **38,** 581–595 (2013).
6. Ng, L. G. *et al.* Migratory dermal dendritic cells act as rapid sensors of protozoan parasites. *PLoS Pathog.* **4,** e1000222 (2008).
7. Turley, S. J. *et al.* Transport of peptide-MHC class II complexes in developing dendritic cells. *Science* **288,** 522–527 (2000).
8. Martln-Fontecha, A. *et al.* Regulation of dendritic cell migration to the draining lymph node: impact on T lymphocyte traffic and priming. *J. Exp. Med.* **198,** 615–621 (2003).
9. Tal, O. *et al.* DC mobilization from the skin requires docking to immobilized CCL21 on lymphatic endothelium and intralymphatic crawling. *J. Exp. Med.* **208,** 2141–2153 (2011).
10. Weber, M. *et al.* Interstitial dendritic cell guidance by haptotactic chemokine gradients. *Science* **339,** 328–332 (2013).
11. Acton, S. E. *et al.* Podoplanin-rich stromal networks induce dendritic cell motility via activation of the C-type lectin receptor CLEC-2. *Immunity* **37,** 276–289 (2012).
12. Pollard, T. D. & Borisy, G. G. Cellular motility driven by assembly and disassembly of actin filaments. *Cell* **112,** 453–465 (2003).
13. Lammermann, T. *et al.* Rapid leukocyte migration by integrin-independent flowing and squeezing. *Nature* **453,** 51–55 (2008).
14. Renkawitz, J. *et al.* Adaptive force transmission in amoeboid cell migration. *Nat. Cell Biol.* **11,** 1438–1443 (2009).
15. Faure-André, G. *et al.* Regulation of dendritic cell migration by CD74, the MHC class II-associated invariant chain. *Science* **322,** 1705–1710 (2008).
16. Heuzé, M. L. *et al.* Migration of dendritic cells: physical principles, molecular mechanisms, and functional implications. *Immunol. Rev.* **256,** 240–254 (2013).
17. Vargas, P., Terriac, E., Lennon-Dumenil, A. M. & Piel, M. Study of cell migration in microfabricated channels. *J. Vis. Exp.* **84,** e51099 (2014).

18. Barton, G. M. & Medzhitov, R. Toll-like receptor signaling pathways. *Science* **300,** 1524–1525 (2003).
19. Heit, B. & Kubes, P. Measuring chemotaxis and chemokinesis: the under-agarose cell migration assay. *Sci. STKE* **2003,** PL5 (2003).
20. Chabaud, M. *et al.* Cell migration and antigen capture are antagonistic processes coupled by myosin II in dendritic cells. *Nat. Commun.* **6,** 7526 (2015).
21. Bailly, M. *et al.* The F-actin side binding activity of the Arp2/3 complex is essential for actin nucleation and lamellipod extension. *Curr. Biol.* **11,** 620–625 (2001).
22. Blanchoin, L. *et al.* Direct observation of dendritic actin filament networks nucleated by Arp2/3 complex and WASP/Scar proteins. *Nature* **404,** 1007–1011 (2000).
23. Svitkina, T. M. & Borisy, G. G. Arp2/3 complex and actin depolymerizing factor/cofilin in dendritic organization and treadmilling of actin filament array in lamellipodia. *J. Cell Biol.* **145,** 1009–1026 (1999).
24. Koivusalo, M. *et al.* Amiloride inhibits macropinocytosis by lowering submembranous pH and preventing Rac1 and Cdc42 signaling. *J. Cell Biol.* **188,** 547–563 (2010).
25. Nolen, B. J. *et al.* Characterization of two classes of small molecule inhibitors of Arp2/3 complex. *Nature* **460,** 1031–1034 (2009).
26. Goley, E. D. *et al.* An actin-filament-binding interface on the Arp2/3 complex is critical for nucleation and branch stability. *Proc. Natl Acad. Sci. USA* **107,** 8159–8164 (2010).
27. Higashida, C. *et al.* Actin polymerization-driven molecular movement of mDia1 in living cells. *Science* **303,** 2007–2010 (2004).
28. Li, F. & Higgs, H. N. The mouse Formin mDia1 is a potent actin nucleation factor regulated by autoinhibition. *Curr. Biol.* **13,** 1335–1340 (2003).
29. Pruyne, D. *et al.* Role of formins in actin assembly: nucleation and barbed-end association. *Science* **297,** 612–615 (2002).
30. Rizvi, S. A. *et al.* Identification and characterization of a small molecule inhibitor of formin-mediated actin assembly. *Chem. Biol.* **16,** 1158–1168 (2009).
31. Eisenmann, K. M. *et al.* T cell responses in mammalian diaphanous-related formin mDia1 knock-out mice. *J. Biol. Chem.* **282,** 25152–25158 (2007).
32. Sakata, D. *et al.* Impaired T lymphocyte trafficking in mice deficient in an actin-nucleating protein, mDia1. *J. Exp. Med.* **204,** 2031–2038 (2007).
33. Tanizaki, H. *et al.* Rho-mDia1 pathway is required for adhesion, migration, and T-cell stimulation in dendritic cells. *Blood* **116,** 5875–5884 (2010).
34. Bovellan, M. *et al.* Cellular control of cortical actin nucleation. *Curr. Biol.* **24,** 1628–1635 (2014).
35. Peng, J., Wallar, B. J., Flanders, A., Swiatek, P. J. & Alberts, A. S. Disruption of the Diaphanous-related formin *Drf1* gene encoding mDia1 reveals a role for Drf3 as an effector for Cdc42. *Curr. Biol.* **13,** 534–545 (2003).
36. Machesky, L. M. *et al.* Scar, a WASp-related protein, activates nucleation of actin filaments by the Arp2/3 complex. *Proc. Natl Acad. Sci. USA* **96,** 3739–3744 (1999).
37. Luckashenak, N., Wahe, A., Breit, K., Brakebusch, C. & Brocker, T. Rho-family GTPase Cdc42 controls migration of Langerhans cells *in vivo*. *J. Immunol.* **190,** 27–35 (2013).
38. Sarris, M. *et al.* Inflammatory chemokines direct and restrict leukocyte migration within live tissues as glycan-bound gradients. *Curr. Biol.* **22,** 2375–2382 (2012).
39. Weber, M. & Sixt, M. Live cell imaging of chemotactic dendritic cell migration in explanted mouse ear preparations. *Methods Mol. Biol.* **1013,** 215–226 (2013).
40. Hawkins, R. J. *et al.* Pushing off the walls: a mechanism of cell motility in confinement. *Phys. Rev. Lett.* **102,** 058103 (2009).
41. Wilson, K. *et al.* Mechanisms of leading edge protrusion in interstitial migration. *Nat. Commun.* **4,** 2896 (2013).
42. Fournier, J. *et al.* Remodeling of the infection chamber before infection thread formation reveals a two-step mechanism for rhizobial entry into the host legume root hair. *Plant Physiol.* **167,** 1233–1242 (2015).
43. French, A. S. *et al.* Dual mechanism for bitter avoidance in *Drosophila*. *J. Neurosci.* **35,** 3990–4004 (2015).

DOI: 10.1038/ncb3284

METHODS

Cells. Mouse bone marrow-derived dendritic cells (BMDCs) were obtained by culturing bone marrow precursors for 10–12 days in IMDM medium containing FCS (10%), glutamine (20 mM), penicillin–streptomycin (100 U ml^{-1}), 2-ME (50 μM) and further supplemented with granulocyte-macrophage colony-stimulating factor (50 ng ml^{-1})-containing supernatant obtained from transfected J558 cells, as previously described[15]. iDCs were obtained by gentle recovery of semi-adherent cells from culture dishes. Mature DCs were obtained by treating iDCs with LPS (100 ng ml^{-1}) for 30 min and washing 3 times with complete medium. LPS-DC migration was recorded between 6 and 16 h post LPS treatment.

BMDCs and mice. LifeAct–GFP and CCR7KO BMDCs were originated from precursors purified from LifeAct–GFP and CCR7KO mice, and were a gift from M. Sixt (IST, Austria)[44,45]. mDia1KO BMDCs were obtained from precursors purified from mDia1KO mice that were generated in A.S.A.'s laboratory (Van Andel Institute)[35]. MyD88KO BMDCs were generated from precursors purified from MyD88KO mice (B6.129-MyD88 tm1*) and obtained from CDTA. Arpc2KO BMDCs were differentiated from precursors obtained from conditional tamoxifen-inducible Arpc2KO mice that were generated as follows: ARPC2FRT/LoxP mice were crossed to FLPeR mice to generate ARPC2 Loxp/+ animals in which the LacZ and neomycin genes had been deleted. ARPC2 Loxp/+ mice were crossed to EsrCre mice to generate ARPC2Loxp/+ EsrCre mice. These animals were crossed to Rosa26-targeted mice containing membrane-targeted tdTomato and membrane-targeted EGFP (mT/mG) reporter genes (Jackson Laboratory) to generate ARPC2Loxp/Loxp CreER mTmG mice. In these animals, tamoxifen-inducible Cre expression triggers both the depletion of Arpc2 and the exchange between tdTomato and GFP reporters, allowing the identification of recombined cells as GFP-positive[46]. This system was used to deplete Arpc2 *in vitro* from BMDC cultures by adding tamoxifen to bone marrow cultures from day 2–8. BMDCs KO for Cdc42 and RhoAKO were generated from mice obtained from T.B's laboratory. Cdc42KO animals were produced as previously described[37]. RhoAKO mice were generated following the same procedure as Cdc42KO mice. All animals are on a C57BL/B6 background and the corresponding breeding controls were systematically used. The experiments were performed on 6–8-week-old male or female mice. For animal care, we strictly followed the European and French National Regulation for the Protection of Vertebrate Animals used for Experimental and other Scientific Purposes (Directive 2010/63; French Decree 2013-118). The present experiments, which used mouse strains exhibiting non-harmful phenotypes, did not require a project authorization and benefited from guidance of the Animal Welfare Body, Research Centre, Institut Curie.

Antibodies and reagents. The following antibodies were used for immunofluorescence (IF) and immunoblot (western blot, WB) experiments: anti-Arpc2 (Millipore, 07-227, WB 1:500), -Arpc4 (Abcam, ab110770, WB 1:500), -Arp2 (Abcam, ab47654, IF 1:50), -Arp3 (Sigma, A5979, WB 1:500), -mDia1 (BD, 610849, IF 1:50, WB 1:200), -GFP (Sigma, GSN149, IF 1:100) and -tubulin (Serotec, MCA77G, WB 1:2,000). For FACS analysis anti-CD11c (HL3, 1:200), -CD86 (GL1, 1:200) and -CD40 (HM40-3, 1:200) were used (BD Biosciences). CCR7 expression was analysed by sequential incubation of DCs with mouse CCL19-Fc (eBioscience, 1:200) and a secondary anti-Fc antibody (Life Technologies, 1:400). To image DCs in micro-channels, we used Ovalbumin AlexaFluor-647 (0.4 mg ml^{-1}), and Hoechst 33342 (200 ng ml^{-1}) (Life Technologies). Pertussis toxin, CK666, Smifh2 and ML141 were obtained from Tocris Bioscience. Cell permeant C3 transferase was obtained from Cytoskeleton. BMDCs were activated using LPS from *Salmonella enterica* serotype typhimurium (Sigma).

Preparation of micro-channels. Micro-channels were prepared as described previously[15,17]. Briefly, polydimethylsiloxane (PDMS) (GE Silicones) was used. Their surface was coated with 10 μg ml^{-1} bovine plasma fibronectin (Sigma) for 1 h and then washed 3 times with PBS before introduction of cells in complete medium.

Velocity measurements in micro-channels. Migrating cells were imaged for 16 h on an epifluorescence video-microscope Nikon TiE microscope equipped with a cooled CCD (charge-coupled device) camera (HQ2, Photometrics) with a ×10 objective. A frequency of acquisition of 1 image per 2 min of transmission phase was used. Kymographs of the migrating cells were generated by subtracting from each frame the mean projection of the whole movie, generating clear objects in a dark background that were analysed using a custom program as described previously[15].

Under-agarose assay. Under-agarose migration was performed as described previously[19]. Briefly, a glass Petri dish was filled with 2 ml of 1.2% warm ultrapure agarose (Gibco) prepared in phenol red-free HBSS (Gibco). After polymerization at 37 °C a small hole was introduced at the centre of the agarose in which Hoechst 33342-stained DCs were loaded similarly to micro-channels experiments. DCs migrating between the agarose and the glass were imaged at ×10 for several hours, tracked following their nucleus and analysed using custom software.

siRNA silencing in BMDCs. BMDCs were transfected with siRNA specific for Arpc4 or mDia1 using the Amaxa mouse Dendritic Cell Nucleofector Kit (Lonza). Briefly, 2 × 10^6 BMDCs collected at day 7 of differentiation were transfected in 100 μl of Amaxa solution containing 10 μM of siRNA (all-star control or target specific). Nucleofected cells were further cultured for 48–72 h in BMDC medium. To test for specific depletion, 4 different siRNAs were tested in a first approach. Two of them were chosen on the basis of their capacity to deplete the corresponding target. LifeAct–GFP localization was evaluated for both siRNAs, but only the one with the highest depletion was chosen to show the data in the article. For mDia1 the siRNAs were obtained from Qiagen (Cat. no. GS13367, Product no. 1027416) and siRNA SI02686390 and SI02666706 were chosen. For Arpc4 the siRNAs were also obtained from Qiagen (Cat. no. GS68089, Product no. 1027416) and siRNA SI05382601 and SI00904141 were chosen.

qPCR. RNA extraction was performed using NucleoSpin RNA (Macherey-Nagel), according to the manufacturer's protocol. cDNA was obtained with the SuperScriptVILO cDNA synthesis kit (Life technologies), according to the manufacturer's protocol, starting from 1 μg of RNA. Quantitative PCR experiments were done with the Lightcycler 480 (Roche) using the Taqman Gene expression assay (Applied Biosystem) with the following primers: Mm01184552_m1 for Arpc4, Mm00492170_m1 for mDia1 and Mm99999915_g1 for GAPDH as a control.

Tamoxifen-induced depletion of Arpc2 gene. At day 4 of culture, bone marrow cells were seeded at 0.5 × 10^6 cells ml^{-1} in BMDC medium containing 1 μM tamoxifen (Sigma). This procedure was repeated at day 7 and cells were further cultured until day 10–11. The cells that had successfully recombined were identified as GFP-positive (∼50% of the cell). To evaluate the efficiency of *Arpc2* gene depletion, GFP$^+$ cells were isolated by FACS sorting and analysed for the expression of Arpc2 by immunoblot. About 75% gene depletion was usually obtained.

Macropinocytosis in migrating DCs. LifeAct–GFP DCs were incubated for 30 min in 200 ng ml^{-1} Hoechst 33342, washed and resuspended in BMDC medium containing 0.4 mg of ovalbumin (OVA) coupled to Alexa-647 (OVA–647). DCs were loaded in micro-channels and their nucleus, actin cytoskeleton and macropinosomes were simultaneously imaged on a Nikon TiE video-microscope with a ×20 objective. The LifeAct–GFP signal was used to generate a mask for each cell. This mask was used to measure the amount of OVA–647 located at the front of the nucleus with a custom ImageJ program to determine the amount of macropinocytosed material. The size and number of macropinosomes were evaluated by imaging cells at their central plane at ×100 magnification on an inverted spinning-disc confocal Roper/Nikon microscope.

LifeAct–GFP imaging and density maps. BMDCs generated from LifeAct–GFP knock-in mice were loaded in micro-channels and imaged for 6 h at 20× using an epifluorescence Nikon TiE video-microscope equipped with a cooled CCD camera (HQ2, Photometrics). On movie reconstruction, individual cells migrating in the channels were cropped using the ImageJ software. To map the LifeAct–GFP signal, the images obtained for each individual cell were aligned in a single column. Cell size normalization was applied to each time point according to the mean cell size and background subtraction. To obtain the mean behaviour of the cell, every time point was projected on average. The mean behaviour of the population was next obtained by projecting the mean signal of every individual cell (Supplementary Fig. 2). This procedure was performed using an ImageJ-compatible custom macro.

Immunofluorescence in micro-channels. Migrating BMDCs were allowed to migrate in micro-channels for 16 h. Cells were fixed with 4% paraformaldehyde (PFA) for 30 min at room temperature and blocked with PBS–2% BSA for 1 h. After blocking, the PDMS was carefully separated from the coverslip that formed the bottom part of the channel and on which most cells remained attached. Cells were next permeabilized with PBS containing 0.2% BSA and 0.05% saponin for 10 min and stained by sequential incubations with primary and secondary antibodies diluted in the permeabilization buffer. Slides were mounted using DAPI Fluoromount-G (SouthernBiotech) and visualized on an inverted spinning-disc confocal Roper/Nikon microscope with a 100× 1.4 NA oil immersion objective. In the case of Arp2 and mDia1 immunostaining, after PFA fixation cells were incubated with cold methanol for 30 s and then permeabilized using 0.02% Triton X-100 for 2 min before staining. To map Arp2 and mDia1 together with LifeAct–GFP signal DCs were stained with an anti-GFP antibody. Unfortunately, methanol fixation disrupted the actin patch observed in live LPS-DCs. To map Arp2 and mDia1 localization cells were imaged at ×20 using an epifluorescence Nikon TiE video-microscope and overlapped as described.

Immunoblotting. DCs were lysed for 2 min in a buffer containing 100 mM Tris, 150 mM NaCl, 0.5% NP-40 and a protease inhibitor cocktail tablet (Roche). Fifty micrograms of soluble extracts were loaded onto a 4–20% TGX gradient gel (BioRad) and transferred onto a Trans-Blot Turbo PVDF/Nitrocellulose membrane (BioRad). The membrane was blocked, incubated sequentially with the appropriate antibodies and revealed using the SuperSignal West Dura substrate (Thermo Scientific). Membranes were cut accordingly to the molecular weight of the protein of interest. This allowed us to evaluate different labelling in the same run. As consequence, full membranes were in most cases only fragments (Supplementary Fig. 8).

Migration in collagen gels. Collagen experiments were performed as described previously[47]. DCs were mixed at 4 °C with 1.6% bovine collagen type I (Advanced BioMatrix) at basic pH. Forty microlitres of the mix was deposited on a 35 mm glass -bottom dish and the drop was homogenized while covered with a 12 mm glass slide. The sample was incubated at 37 °C for 20 min to allow collagen polymerization. To generate the CCL21 gradient, 2 ml of BMDC medium containing 200 ng ml^{-1} of CCL21 was added to the plate. Cells were imaged (phase contrast) at a frequency of 1 image per 2 min using a ×10 objective overnight. Contiguous positions were stitched using the FIJI plugin Grid/collection stitching[48] and images were processed to extract cell tracks. The mean image of the movie was subtracted from every time point and white objects in a dark background were detected. Resulting movies were processed using the FIJI plugin Filter Mean (Intensity 3) and cells were tracked using custom software[49].

Migration in ear explants. Migration of DCs was performed as recently described, but modified to work with classic multi-position epifluorescence inverted microscopes[39]. Briefly, the epidermal sheet of isolated mice ears was removed, exposing the dermal part located just under the skin. After isolation, the dermal side was incubated sequentially with rat-anti Lyve1 (R&D) and anti-rat Alexa647 (Life technologies) for 1 h at 4 °C. CFSE (Life technologies) or CMTMR (Life technologies)-coloured LPS-DCs were added on top of the exposed dermal side of the skin for 1 h. Loosely attached cells were washed off and ears mounted on a PDMS block that kept the tissue flat. The block was inverted on top of a glass plate and immobilized to allow long-lasting cell recording on an epifluorescence Nikon TiE video-microscope equipped with a cooled CCD camera (HQ2, Photometrics). Tracks of migratory cells were obtained using the FIJI plugin MTrackJ.

Tracking analysis of ears DC migration. To analyse cell trajectories, custom C++ routines coupled with R (ref. 50) were developed[51]. The mean square displacement (MSD) was computed and fitted as previously described[51]. The squared distance between every two points of a cell track separated by a specific time lag was averaged over the entire population of trajectories. MSDs are ultimately plotted as a function of increasing time lag. The path persistence of a trajectory was defined as the ratio between the length of the cell path and the diameter of the theoretical disc containing the entire trajectory. It tends to 1 for very persistent tracks and to 0 for cells continuously changing their direction.

DCs homing to LNs. BMDCs generated from mDia1WT and KO mice were concentrated at 10×10^6 cells ml^{-1} in serum-free media and labelled for 10 min at 37 °C with either 2.5 μM CFSE (Invitrogen) or 2.5 μM CMTMR (Invitrogen) before stopping the reaction with complete medium. We stimulated BMDCs with 100 ng ml^{-1} LPS for 30 min at 37 °C, washed them twice and mixed them in equal numbers. Then, 20 μl of the mixed cell suspension containing 2×10^6 cells of each genotype was injected into the footpad of recipient C57BL/6 mice and 16 h later popliteal lymph nodes were collected, dissected and digested by incubating with 1 mg ml^{-1} collagenase D (Roche) for 30 min. To rule out any dye-specific effects, in each experiment cells from both genotypes were labelled by exchanging dies. For each genotype we calculated the homing index as the ratio of $CFSE_{LN}/CMTMR_{LN}$ to $CFSE_{Input}/CMTMR_{Input}$ to determine relative migratory capacity (LN: lymph node).

Statistics and reproducibility. Most of the experiments shown in figures correspond to representative experiments in which *n* cells were analysed as indicated in the legends. Migration experiments typically contained 40–100 cells per condition. An internal control (iDCs compared with LPS-DCs) was included in each migration experiment. Each experiment validated based on this internal control was repeated two or three times and conclusions were made only when results were reproduced in each individual experiment. Immunofluorescence experiments were systematically quantified using unbiased methods applied to data obtained from at least two independent experiments. In general, statistical comparison of internal samples was carried out using the non-parametric Mann–Whitney test except in collagen assays where the number of cells was extremely high (more than 2,000 tracks). In that case tracks were randomly selected and analysed with the appropriate statistical test (see figure legends). No statistical method was used to predetermine sample size. The experiments were not randomized and the investigators were not blinded to allocation during experiments and outcome assessment.

44. Forster, R. *et al.* CCR7 coordinates the primary immune response by establishing functional microenvironments in secondary lymphoid organs. *Cell* **99,** 23–33 (1999).
45. Riedl, J. *et al.* Lifeact mice for studying F-actin dynamics. *Nat. Methods* **7,** 168–169 (2010).
46. Muzumdar, M. D., Tasic, B., Miyamichi, K., Li, L. & Luo, L. A global double-fluorescent Cre reporter mouse. *Genesis* **45,** 593–605 (2007).
47. Wolf, K. *et al.* Physical limits of cell migration: control by ECM space and nuclear deformation and tuning by proteolysis and traction force. *J. Cell Biol.* **201,** 1069–1084 (2013).
48. Preibisch, S., Saalfeld, S. & Tomancak, P. Globally optimal stitching of tiled 3D microscopic image acquisitions. *Bioinformatics* **25,** 1463–1465 (2009).
49. Maiuri, P. *et al.* The first world cell race. *Curr. Biol.* **22,** R673–R675 (2012).
50. R-Core-Team. *R: A Language and Environment for Statistical Computing* (R Foundation for Statistical Computing, 2014); http://www.r-project.org
51. Selmeczi, D., Mosler, S., Hagedorn, P. H., Larsen, N. B. & Flyvbjerg, H. Cell motility as persistent random motion: theories from experiments. *Biophys. J.* **89,** 912–931 (2005).

DOI: 10.1038/ncb3284

nature cell biology

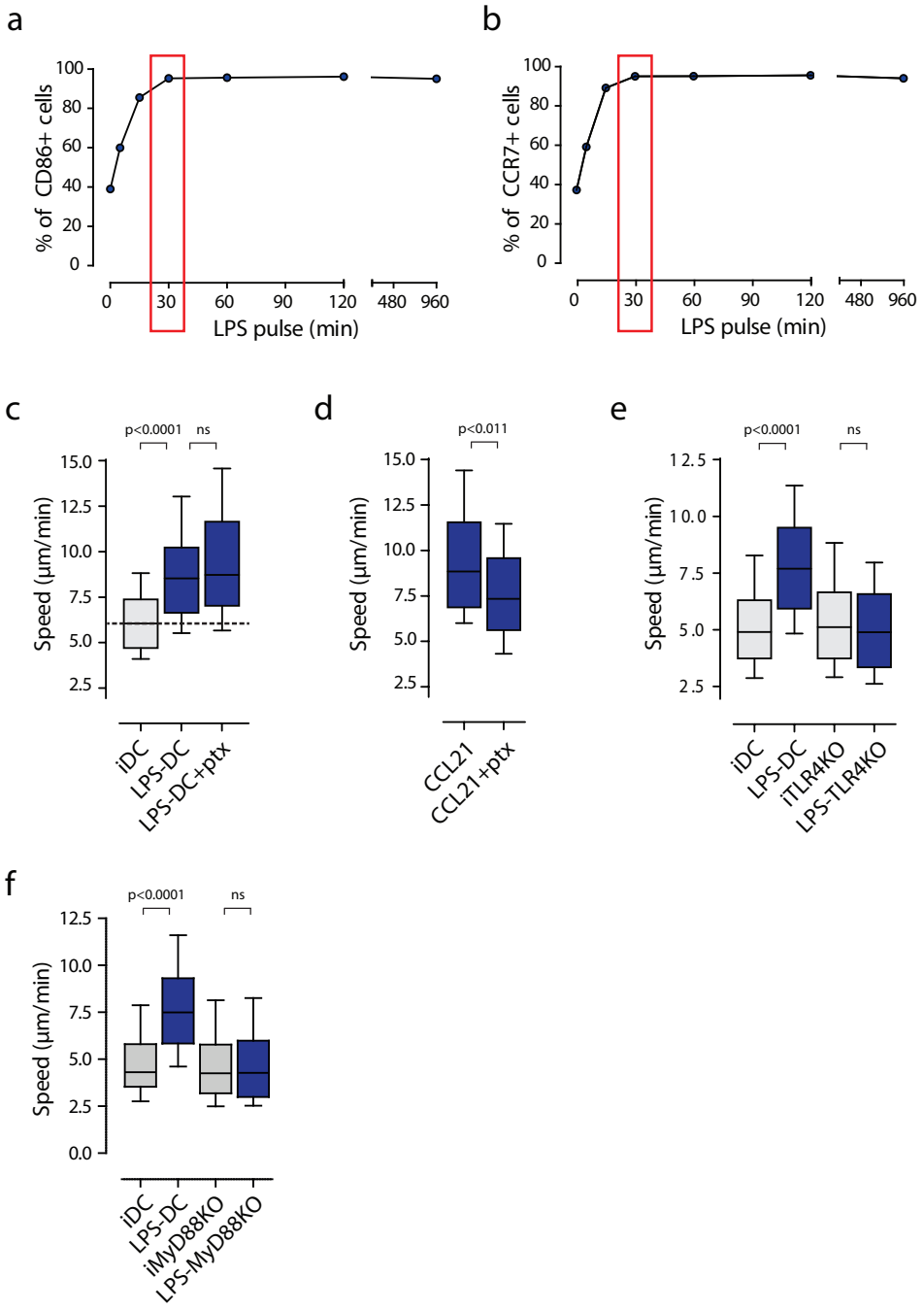

Supplementary Figure 1 DC migration becomes faster and more persistent upon LPS treatment. **a-b,** Analysis by flow cytometry of surface expression of the DC activation marker CD86 and the chemokine receptor CCR7. iDCs were incubated for different times with LPS (100 ng/ml), washed and cultured overnight. 30 min was found to be the minimal time to get the highest level of activation and CCR7 expression. 1 representative experiment out of 3 is shown. **c**, Mean instantaneous speed of migrating DCs in the presence of Pertussis toxin (Ptx, 200 µg/ml) in fibronectin- (c) or fibronectin plus CCL21- (d) coated micro-channels (n= 80, 94 and 91 for iDC, LPS-DC and LPS-DC Ptx respectively). 1 representative experiment out of 2 is shown. **d**, Ptx does not affect the LPS-induced increment in DC speed (c) but decreases the velocity of LPS-DCs migrating in the presence of CCL21 (d) (positive control for the activity of Ptx, n=92 and 100 for CCL21 and CCL21 Ptx respectively). 1 representative experiment out of 2 is shown. **e,** Mean instantaneous speed of WT and TLR4KO DCs migrating in micro-channels (n=150, 150, 152 and 122 for iDC, LPS-DC, iTLR4KO and LPS-TLR4KO cells respectively). 1 representative experiment out of 2 is shown. **f,** Mean instantaneous speed of control and Myd88KO DCs migrating in micro-channels (n=81, 74, 67 and 102 for iDC, LPS-DC, iMyd88KO and LPS-Myd88KO respectively). 1 representative experiment out of 3 is shown. The Mann-Whitney test was applied for statistical analyses in c-f. In the box plots of panels c-f the bars include 90% of the points, the center corresponds to the median and the box contains 75% of the data.

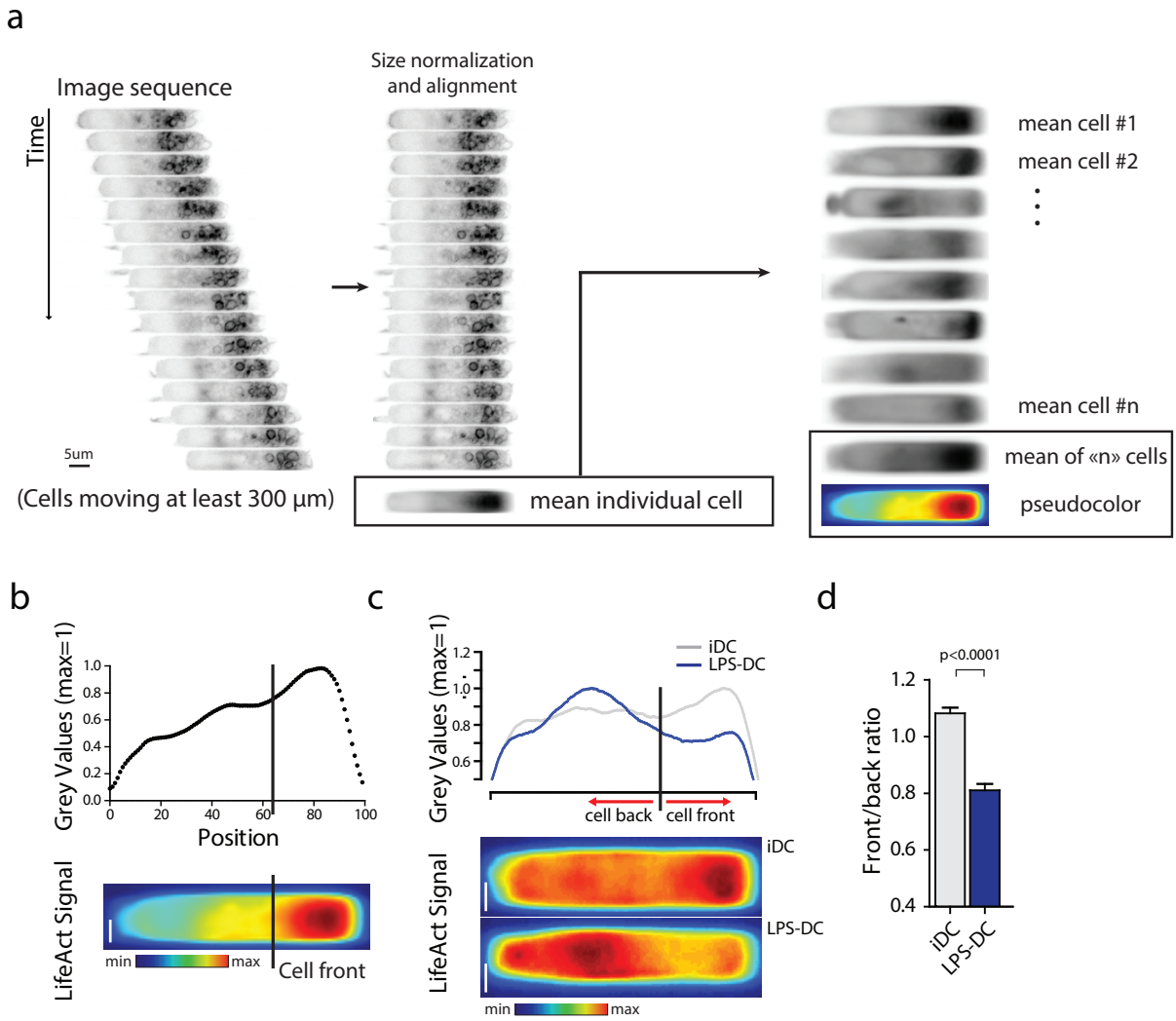

Supplementary Figure 2 Quantification of LifeAct-GFP dynamics in migrating DCs. **a-b,** Method used to quantify LifeAct-GFP localization in migrating DCs. Sequential images of LifeAct-GFP DCs were acquired on an epifluorescence microscope every 1min at 20x. Scale bar: 10µm. **a,** The LifeAct-GFP signal recorded at each time-point was integrated into a single image for all migrating cells. Cell alignment and cell size normalization were applied to generate the LifeAct-GFP density maps. Scale bar: 5 µm. **b**, Mean intensities obtained for each cell were averaged into a single LifeAct-GFP density map, assigning equivalent weight to each cell. Scale bar: 2.5 µm. **c-d,** Analysis of the LifeAct-GFP front/back ratio in iDCs and LPS-DCs migrating in micro-channels. The front was defined as the first third of the cell. Scale bar: 2.5 µm. Results obtained by analyzing the data showed in Fig. 2a-c (n=31 and 27 cells for iDC and LPS-DC respectively). 1 representative experiment out of 4 is shown. Graphic shows mean and error bars correspond to S.E.M. The Mann-Whitney test was applied for all statistical analysis.

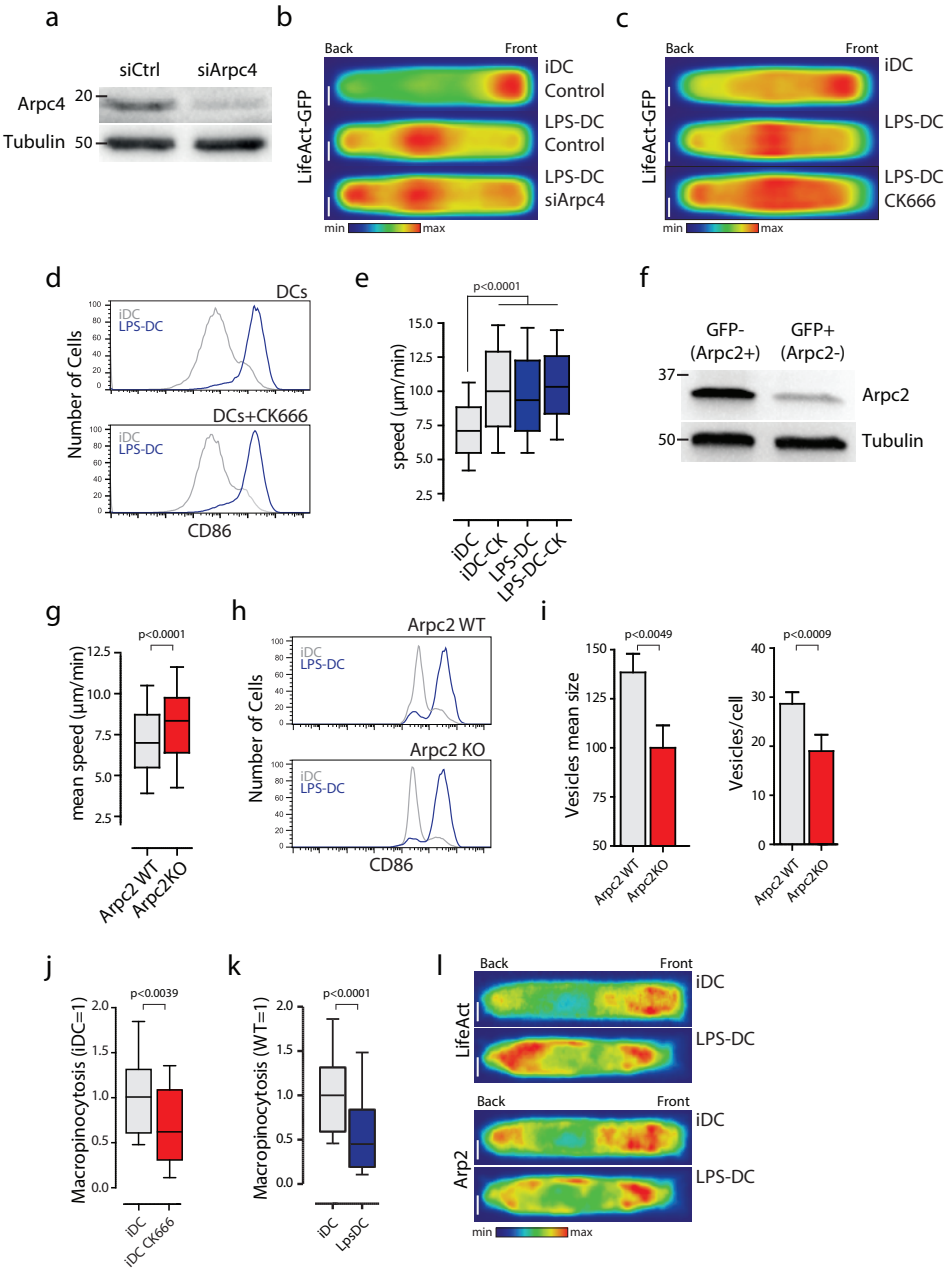

Supplementary Figure 3 Arp2/3 decreases the migration of iDCs but enhances their antigen uptake capacity. **a,** Immunoblot blot analysis of Arpc4 expression in BMDCs nucleofected with Arpc4-specific siRNA. **b, c,** LifeAct-GFP density maps obtained from iDC or LPS-DC silenced (**b**) or inhibited (**c**) for Arp2/3. LPS-DCs were treated with the Arp2/3 inhibitor CK666 (25 μM) or silenced for Arpc4. Scale bar: 2.5 μm. 1 representative experiment out of 2 is shown. **d,** Analysis by flow cytometry of surface expression of the DC activation marker CD86. iDCs were incubated 30 min with LPS (100 ng/ml), washed and cultured overnight. 1 experiment out of 4 is shown. **e**, Mean instantaneous speed of DCs migrating in micro-channels and treated or not with CK666 as in c (n=244, 192, 231 and 230 for iDC, iDC-CK666, LPS-DC and LPS-DC CK666 respectively). 1 representative experiment out of 3 is shown. **f**, Immunoblot analysis of Arpc2 and tubulin expression in tamoxifen-treated DCs. TomatoFP$^+$ (Arpc2WT) and conditional GFP$^+$ (Arpc2KO) iDCs were sorted from 10-days- DC cultures in which tamoxifen was added during the last 8 days. **g,** Analysis of the migration of Arpc2WT and KO iDCs under an agarose gel. Cells were imaged during 200 min and their cell speed was quantified after tracking. The analysis was performed on cells that had migrated >100 μm (n= 80 and 163 for Arpc2 WT and Arpc2 KO respectively). 1 representative experiment out of 2 is shown. **h,** Analysis by flow cytometry of surface expression of the DC activation marker CD86 performed as in d. **i**, Quantification of the size (left) and number (right) of vesicles present at the front of Arpc2WT and KO DCs migrating in micro-channels filled with fluorescent ovalbumin (n=36 and 37 for Arpc2WT and Arpc2 KO respectively). Graphics show mean and error bars correspond to S.E.M. **j,** Macropinocytic capacity of migrating DCs treated with the Arp2/3 inhibitor CK666 (n=62 and 41 for iDC and iDC CK666 respectively). 1 representative experiment out of 3 is shown. **k,** Macropinocytic capacity of iDCs and LPS-DCs (n=39 and 33 for iDC and LPS-DC respectively). 1 representative experiment out of 2 is shown. **l,** Density maps obtained from LifeAct-GFP DCs fixed while migrating in micro-channels and stained for Arp2 and GFP. Scale bar: 2.5 μm. In the box plots of panels e, g, j and k the bars include 90% of the points, the center corresponds to the median and the box contains 75% of the data. The Mann-Whitney test was applied for all statistical analyses.

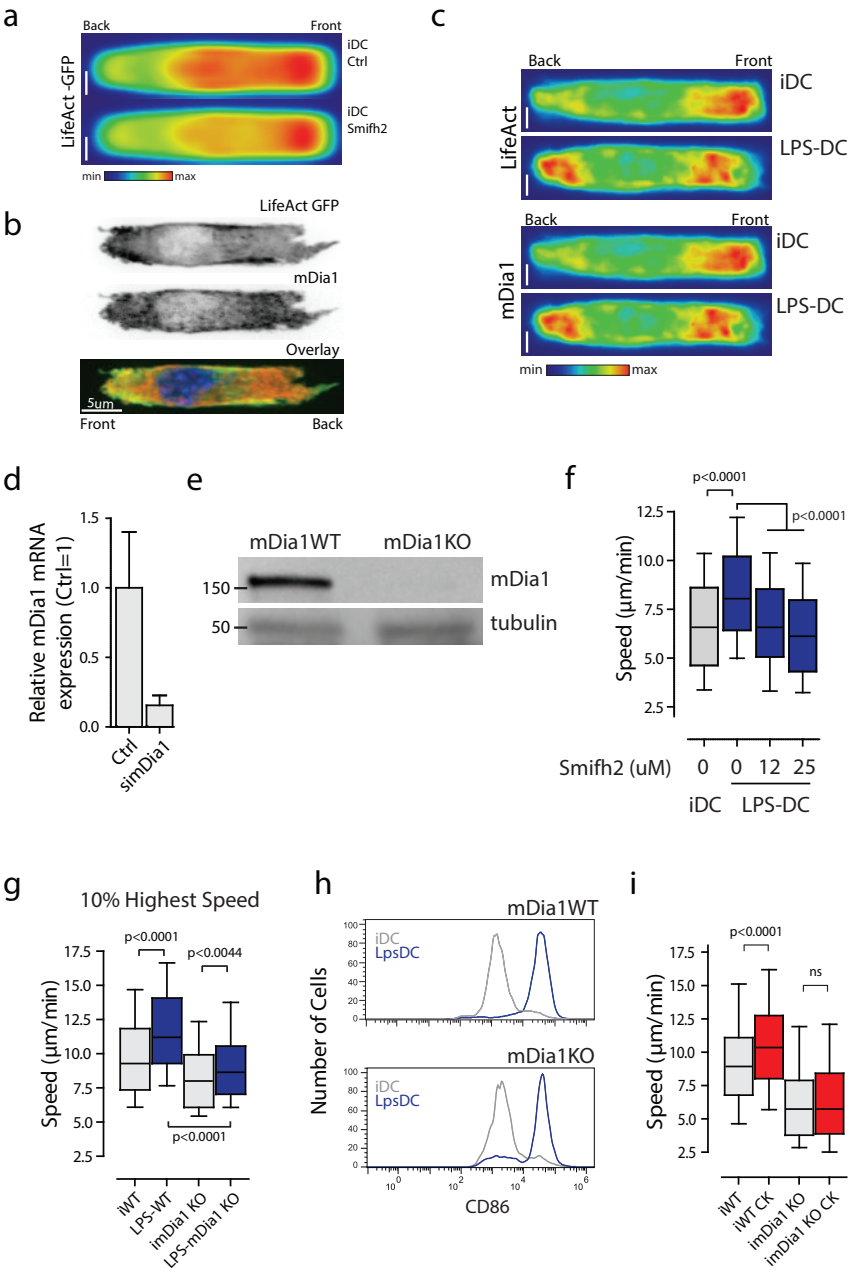

Supplementary Figure 4 Actin distribution at the back of DCs relies on the Formin mDia1 and is required for fast and persistent migration. **a,** LifeAct-GFP density maps of iDCs migrating in the presence or absence of the formin inhibitor Smifh2 (25 µM). 1 representative experiment out of 3 is shown. Scale bar: 2.5 µm. **b,** Immunofluorescence analysis of mDia1 expression in LPS-DCs migrating in micro-channels analyzed by spinning disk microscope (100x). Scale bar: 5 µm. **c**, Density maps obtained from LifeAct-GFP DC fixed while migrating in micro-channels and stained for mDia1 and GFP (2 independent experiments). Scale bar: 2.5 µm. **d**, Quantitative PCR analysis of mDia1 expression in DCs nucleofected with mDia1-specific siRNA. Graphic shows mean and error bars correspond to S.E.M. **e,** Immunoblot analysis of mDia1 and tubulin expression in immature mDia1WT and KO DCs. 1 representative experiment out of 3 is shown. **f,** Mean instantaneous speed of LPS-DCs migrating in micro-channels and treated with different doses of Smifh2 (n=125, 154, 134 and 141 for iDC, LPS-DC, LPS-DC 12 µM and LPS-DC 25 µM respectively). 1 representative experiment out of 3 is shown. **g**, 10% of the highest instantaneous speed values of DCs migrating in micro-channels (n=210, 238, 233 and 179 for iWT, LPS-WT, imDia1KO and LPS-mDia1KO respectively). 1 representative experiment out of 5 is shown. **h,** Analysis by flow cytometry of surface expression of the DC activation marker CD86. iDCs were incubated 30 min with LPS (100 ng/ml), washed and cultured overnight. 1 experiment out of 4 is shown. **i,** Mean instantaneous speed of mDia1WT and KO migrating in micro-channels and treated with CK666 (25 µM) (n=119, 107, 52 and 111 for iWT, iWT CK, imDia1KO and imDia1KO CK respectively). 1 representative experiment out of 2 is shown. In the box plots of panels f, g and i the bars include 90% of the points, the center corresponds to the median and the box contains 75% of the data. The Mann-Whitney test was applied for all statistical analyses.

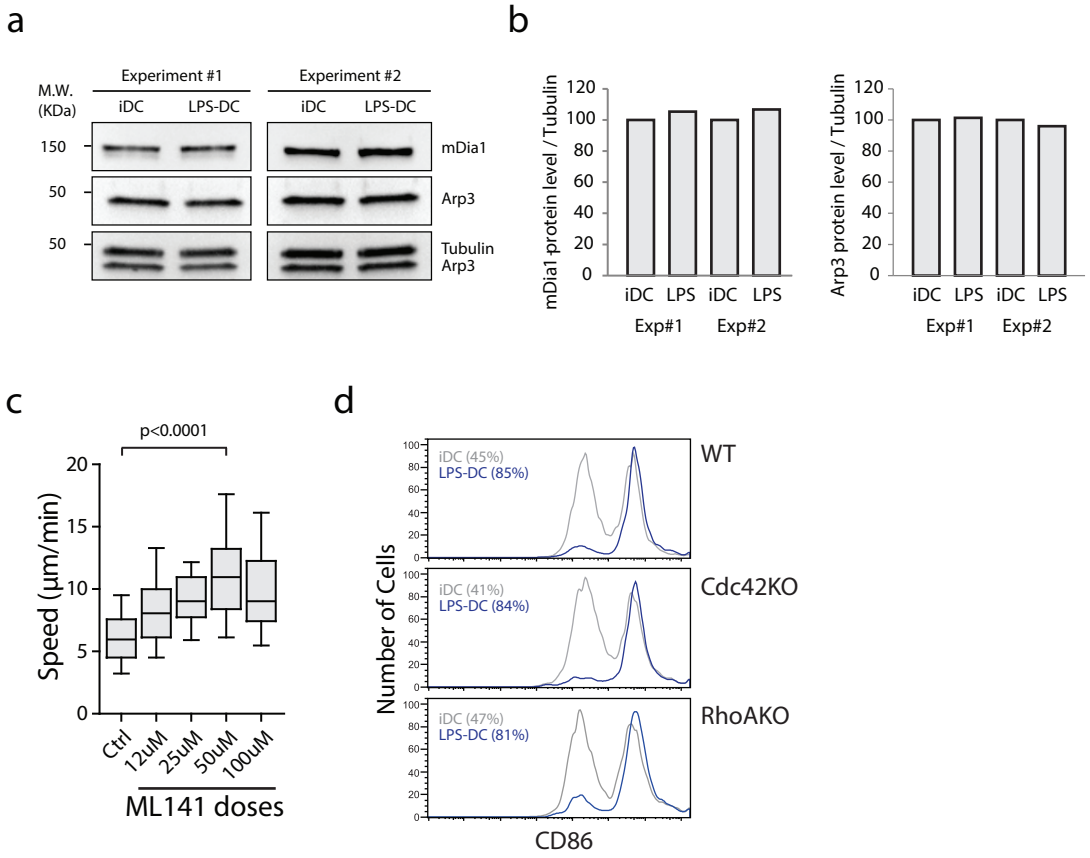

Supplementary Figure 5 Regulation of DC Arp2/3- and mDia1-dependent actin nucleation by Cdc42 and RhoA. **a, b**. iDCs were treated with LPS for 30 min, washed and further cultured at 37°C during 16h. **a**. Immunoblot analysis was performed as described in the supplementary experimental procedures. **b**. Normalized intensity obtained from data showed in panel a. Graphics show mean individual values. **c**, Mean instantaneous speed of iDCs migrating in micro-channels and treated with different doses of ML141 (n=164, 163, 142, 143 and 39 for iDC, iDC 12 µM, iDC 25 µM, iDC 50 µM and iDC 100 µM respectively). 1 experiment out of 3 is shown. In the box plot the bars include 90% of the points, the center corresponds to the median and the box contains 75% of the data. The Mann-Whitney test was applied for statistical analysis. **d**, Analysis by flow cytometry of surface expression of the DC activation marker CD86. iDCs were incubated 30 min with LPS (100 ng/ml), washed and cultured overnight.

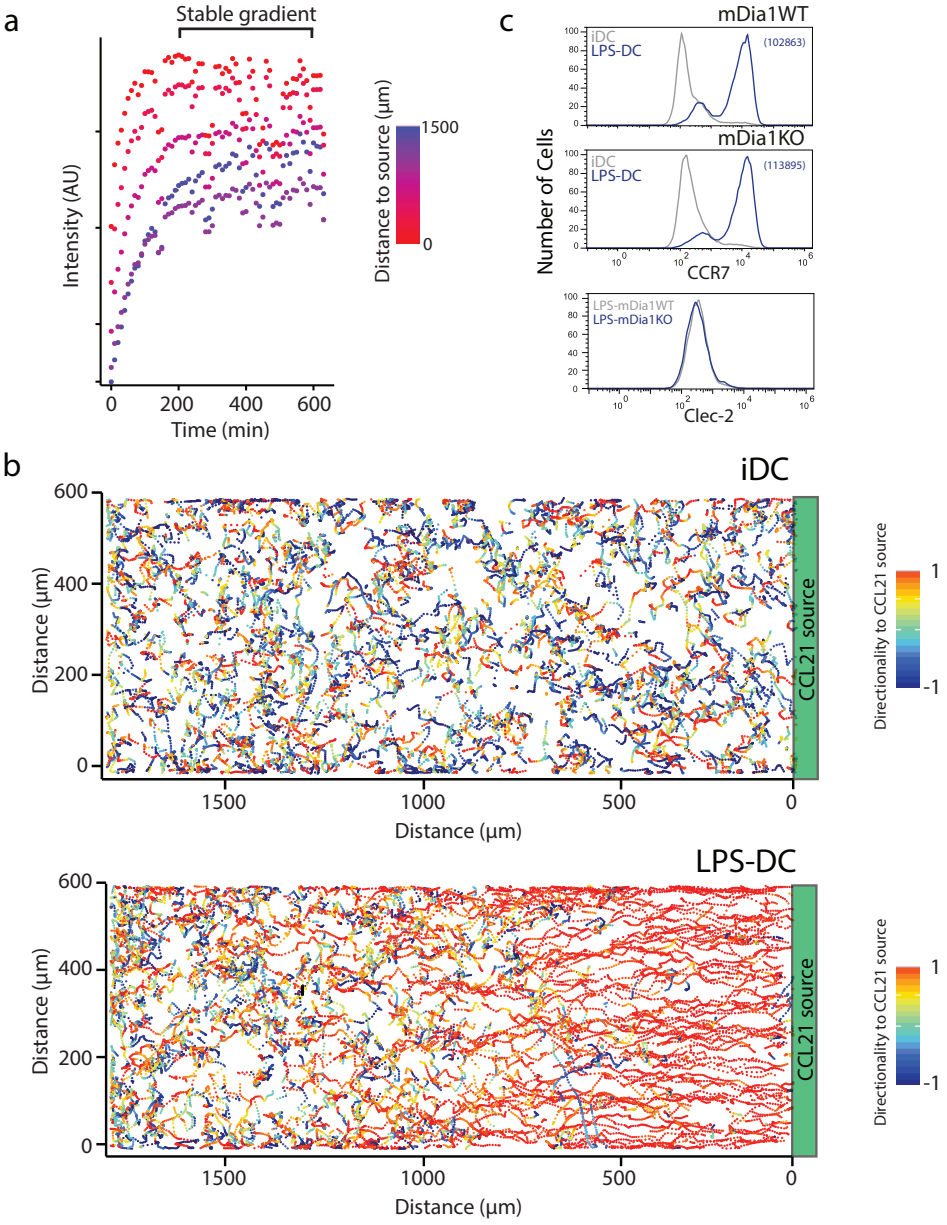

Supplementary Figure 6 Analysis of chemokine gradient sensing by iDCs and LPS-DCs. **a,** Collagen gels were bathed with a solution containing fluorescent ovalbumin (OVA), to evaluate protein penetration in the gel. Gradient steepness was evaluated by measuring the changes in fluorescence intensity according to the protein source using an epifluorescence microscope. Areas closer to the protein source (red) reached a plateau faster than distal areas (blue). After 200 min the gradient was considered as stable at any distance from the source. All the images showed in the paper correspond to analysis between 200 min and 600 min after addition of the chemokine. **b,** CCR7 and Clec-2 surface staining using flow cytometry was performed in DCs treated with LPS (100ng/ml) for 30 min and further cultured overnight. Geometric mean of fluorescence in the CCR7 positive population is depicted. **c**, Trajectories of iDCs (upper panel) and LPS-DCs (lower panel) along the CCL21 gradient formed in collagen gels. Directionality of segments of cell trajectories is shown in different colors: from red (toward the source) to blue (against it).

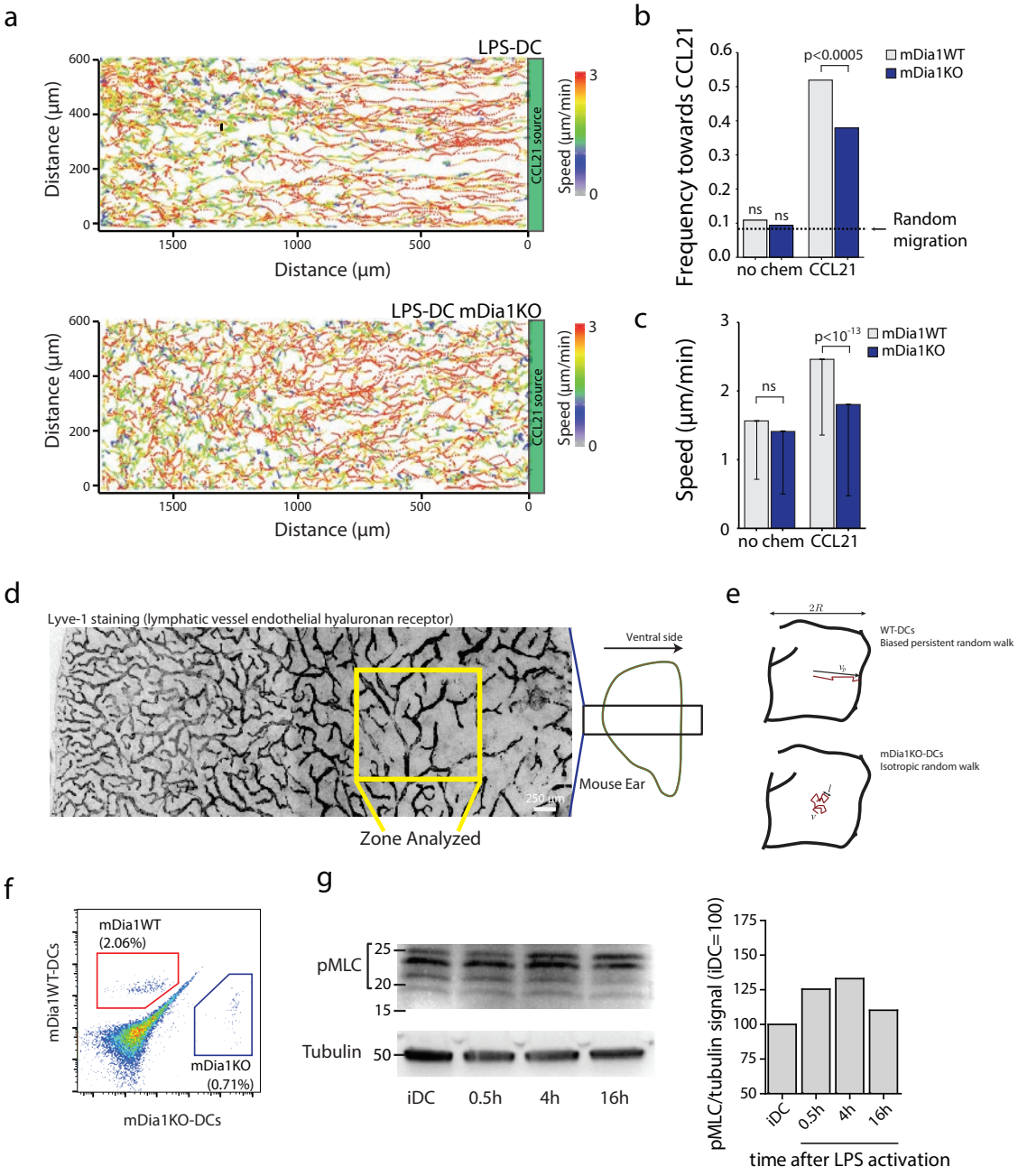

Supplementary Figure 7 Analysis of chemokine gradient sensing by mDia1KO LPS-DCs. **a,** Trajectories of WT (upper panel) and mDia1KO LPS-DCs (lower panel) along the CCL21 gradient formed in collagen gels. Speed of segments of cell trajectories is shown in different colors: from red (fast) to blue (slow). **b,** frequency of movement in the direction of the gradient in the 500 µm closer to the CCL21 source compared to random migration in absence of chemokines. Values are compared to equivalent position in the absence of chemokines. Analysis performed in 500 random tracks due to oversampling. **c**, Mean speed of DCs in the 500 µm closer to the CCL21 source. Analysis performed in 500 random tracks due to oversampling. Error bars correspond to S.D. Student's t-Test was applied for statistical analysis in b. Chi-squared Test was applied for statistical analysis in c. **d,** Ear explant stained with the anti-Lyve-1 marker to highlight LVs. The area enclosed in the yellow square corresponds to the zone analyzed when monitoring DC migration to LVs. Scale bar 250 µm. **e,** Scheme of different types of trajectories representing the behavior of mDia1WT and KO LPS-DCs in the ear explants. **f.** mDia1WT and KO LPS-DCs were stained with CMTRM or CFSE and co-injected in the footpad of WT recipient mice. Their presence in the popliteal lymph node 16 h later was analyzed by flow cytometry. Example representative of 3 experiments is shown. **g**, pMLC levels on DCs activated 30 min with LPS and cultured during the indicated time. The pMLC signal was normalized to tubulin levels.

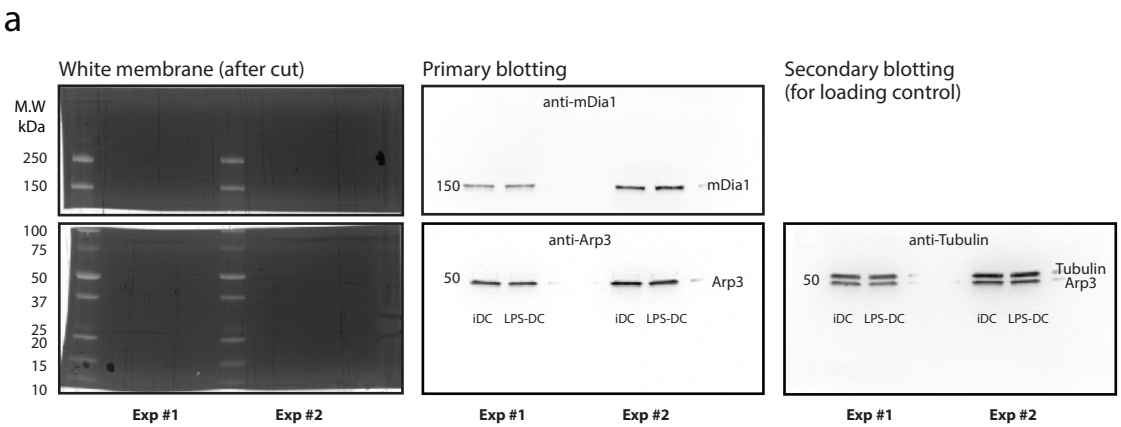

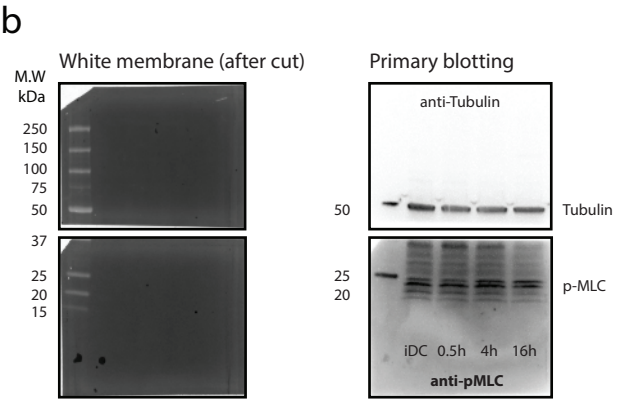

Supplementary Figure 8 Unprocessed full scans of key blots. **a**, Full scans of immunoblots showed in supplementary figure 5a. The whole membrane was divided in two based on the 100 kDa molecular weight marker (left panel). Each blot was sequentially incubated with the indicated primary antibody and the corresponding HRP-conjugated secondary antibody (central panel). For loading controls, the membrane containing the 50 kDa band was incubated sequentially with an anti-tubulin antibody and revealed with the corresponding HRP-conjugated secondary antibody (right panel). **b**, Full scans of immunoblots showed in supplementary figure 7g. Blots were obtained as described in a, except that the gel was cut based on the 37 kDa molecular weight marker, allowing detection of phospho-MLC and tubulin in the same run.

Supplementary Video Legends

Supplementary video 1: Distinct LifeAct-GFP dynamics in iDCs and LPS-DCs
LifeAct-GFP-expressing DCs migrating in 8 µm x 5µm fibronectin-coated micro-channels and time-lapsed on a spinning disk microscope (20x) at a frequency of 1 image/2min. Scale bar 5 µm.

Supplementary video 2: F-actin is enriched in ruffles at the front of iDCs
LifeAct-GFP-expressing iDCs migrating in 8 µm x 5µm fibronectin-coated micro-channels and time-lapsed on a spinning disk microscope (100x) at a frequency of 1 image/400ms. The cortex of a representative cell is shown. Scale bar 5 µm.

Supplementary video 3: F-actin is enriched at the rear of LPS-DCs
LifeAct-GFP-expressing LPS-DCs migrating in 8 µm x 5µm fibronectin-coated micro-channels and time-lapsed on a spinning disk microscope (100x) at a frequency of 1 image/400ms. The cortex of a representative cell is shown. Scale bar 5 µm.

Supplementary video 4: LPS-DCs but not iDCs respond to CCL21 gradients
iDCs and LPS-DC migrating along a CCL21 gradient in a collagen gel. The frequency of acquisition was 1 image/2 min (10x) on a video-microscope. The source of CCL21 is at the right of the movie. Scale bar 50 µm.

Supplementary video 5: Chemotaxis of wild-type and mDia1KO LPS-DCs in vitro
mDia1 wild-type and KO LPS-DCs migrating along a CCL21 gradient in a collagen gel. 1 image/2min (10x) was acquired on a video-microscope. The source of CCL21 is at the right of the movie. Scale bar 50 µm.

Supplementary video 6: Chemotaxis of wild-type and mDia1KO LPS-DCs in vivo
mDia1 wild-type (red) and KO (green) LPS-DCs migrating in an ear explant. 1 image/2min (20x) was acquired on a on a video-microscope. Scale bar 50 µm.